



# 1 CEDAR-GPP: spatiotemporally upscaled estimates of gross primary 2 productivity incorporating CO<sub>2</sub> fertilization

3 Yanghui Kang<sup>1,2</sup>, Max Gaber<sup>1,3</sup>, Maoya Bassiouni<sup>1,2</sup>, Xinchun Lu<sup>1,2</sup>, Trevor F. Keenan<sup>1,2</sup>

4 <sup>1</sup> Department of Environmental Science, Policy, and Management, University of California,  
5 Berkeley, Berkeley, CA 94720, USA

6 <sup>2</sup> Climate and Ecosystem Sciences Division, Lawrence Berkeley National Laboratory,  
7 Berkeley, CA 94720, USA

8 <sup>3</sup> Department of Geosciences and Natural Resource Management, University of  
9 Copenhagen, Copenhagen, 1350, Denmark.

10 Correspondence: Yanghui Kang (yanghuikang@berkeley.edu)

11 Trevor Keenan (trevorkeen@berkeley.edu)

12

13 **Abstract:** Gross primary productivity (GPP) is the largest carbon flux in the Earth system, playing a  
14 crucial role in removing atmospheric carbon dioxide and providing the sugars and starches needed  
15 for ecosystem metabolism. Despite the importance of GPP, however, existing estimates present  
16 significant uncertainties and discrepancies. A key issue is the underrepresentation of the CO<sub>2</sub>  
17 fertilization effect, a major factor contributing to the increased terrestrial carbon sink over recent  
18 decades. This omission could potentially bias our understanding of ecosystem responses to climate  
19 change.

20 Here, we introduce CEDAR-GPP, the first global upscaled GPP product that incorporates  
21 the direct CO<sub>2</sub> fertilization effect on photosynthesis. Our product is comprised of monthly GPP  
22 estimates and their uncertainty at 0.05° resolution from 1982 to 2020, generated using a  
23 comprehensive set of eddy covariance measurements, multi-source satellite observations, climate  
24 variables, and machine learning models. Importantly, we used both theoretical and data-driven  
25 approaches to incorporate the direct CO<sub>2</sub> effects. Our machine learning models effectively predicted  
26 monthly GPP ( $R^2 \sim 0.74$ ), the mean seasonal cycles ( $R^2 \sim 0.79$ ), and spatial variabilities ( $R^2 \sim 0.67$ ).  
27 Incorporation of the direct CO<sub>2</sub> effects substantially improved the models' ability to estimate long-  
28 term GPP trends across global flux sites. While the global patterns of annual mean GPP, seasonality,



29 and interannual variability generally aligned with existing satellite-based products, CEDAR-GPP  
30 demonstrated higher long-term trends globally after incorporating CO<sub>2</sub> fertilization, particularly in  
31 the tropics, reflecting a strong temperature control on direct CO<sub>2</sub> effects. CEDAR-GPP offers a  
32 comprehensive representation of GPP temporal and spatial dynamics, providing valuable insights  
33 into ecosystem-climate interactions. The CEDAR-GPP product is available at  
34 <https://doi.org/10.5281/zenodo.8212707> (Kang et al., 2023).  
35



## 36 1. Introduction

37 Terrestrial ecosystem photosynthesis, known as Gross Primary Productivity (GPP), is the  
38 primary source of food and energy for the Earth system and human society. Through  
39 photosynthesis, terrestrial ecosystems also mitigate climate change, by removing thirty percent of  
40 anthropogenic carbon emissions from the atmosphere each year (Friedlingstein et al., 2023).  
41 However, due to the lack of direct measurements at the global scale, our understanding of  
42 photosynthesis and its spatiotemporal dynamics is limited, leading to considerable disagreements  
43 among various GPP estimates (Anav et al., 2015; Smith et al., 2016; O’Sullivan et al., 2020; Yang et  
44 al., 2022). Addressing these uncertainties is crucial for improving the predictability of ecosystem  
45 dynamics under climate change (Friedlingstein et al., 2014).

46 Over the past three decades, global networks of eddy covariance flux towers collected *in situ*  
47 carbon flux measurements that allow for accurate estimates of GPP, providing valuable insights into  
48 photosynthesis dynamics under various environmental conditions (Baldocchi, 2020; Beer et al.,  
49 2010). To quantify and understand GPP at scales and locations beyond the  $\sim 1\text{km}^2$  flux tower  
50 footprints, machine learning has been employed with gridded satellite and climate datasets to upscale  
51 site-based measurements and produce wall-to-wall GPP maps (Yang et al., 2007; Xiao et al., 2008;  
52 Jung et al., 2011; Tramontana et al., 2016; Joiner and Yoshida, 2020; Zeng et al., 2020; Dannenberg  
53 et al., 2023). This approach provides important observational constraints of global carbon dynamics,  
54 complementing process-based and semi-process-based modeling such as terrestrial biosphere  
55 models or the Light Use Efficiency (LUE) models (Beer et al., 2010; Jung et al., 2017; Schwalm et  
56 al., 2017; Gampe et al., 2021).

57 Effective machine learning upscaling depends on a complete set of input predictors that fully  
58 explain GPP dynamics. Upscaled datasets have primarily relied on satellite-observed greenness  
59 indicators, such as vegetation indexes, Leaf Area Index (LAI), the fraction of absorbed  
60 photosynthetically active radiation (fAPAR), which effectively capture canopy-level GPP dynamics  
61 related to leaf area changes (Tramontana et al., 2016; Ryu et al., 2019; Joiner and Yoshida, 2020).  
62 However, important aspects of leaf-level physiology, such as those controlled by climate factors, are  
63 often omitted in major upscaled datasets, preventing accurate characterization of GPP responses to  
64 climate change (Stocker et al., 2019; Bloomfield et al., 2023). In particular, none of the previous  
65 upscaled datasets have considered the direct effect of atmospheric  $\text{CO}_2$  on leaf-level photosynthesis,  
66 which is a key factor contributing to at least half of the enhanced land carbon sink observed over the



67 past decades (Keenan et al., 2016; Keenan and Williams, 2018; Walker et al., 2021; Ruehr et al.,  
68 2023). This omission can lead to incorrect inferences regarding long-term trends in various  
69 components of the terrestrial carbon cycle (De Kauwe et al., 2016).

70 Multiple independent lines of evidence from the atmospheric inversion (Wenzel et al., 2016),  
71 atmospheric  $^{13}\text{C}/^{12}\text{C}$  measurements (Keeling et al., 2017), ice core records of carbonyl sulfide  
72 (Campbell et al., 2017), glucose isotopomers (Ehlers et al., 2015), as well as free-air  $\text{CO}_2$  enrichment  
73 experiments (FACE) (Walker et al., 2021), suggest a widespread positive effect of elevated  
74 atmospheric  $\text{CO}_2$  on GPP from site to global scales. Increasing  $\text{CO}_2$  *directly* stimulates the  
75 biochemical rate of leaf-level photosynthesis, leading to an increase in net carbon assimilation and  
76 leaf area, which enhances canopy-level GPP. Furthermore, high  $\text{CO}_2$  concentration is expected to  
77 reduce stomatal conductance and increase water use efficiency, indirectly enhancing photosynthesis  
78 under water-limited conditions (De Kauwe et al., 2013; Keenan et al., 2013). The direct biochemical  
79 effect has been found to dominate GPP responses to  $\text{CO}_2$ , from both theoretical and observational  
80 analyses (Haverd et al., 2020; Chen et al., 2022).

81 Satellite-based estimates have shown an increasing global GPP trend in the past few decades  
82 largely attributable to  $\text{CO}_2$ -induced increases in LAI (De Kauwe et al., 2016; Zhu et al., 2016; Chen  
83 et al., 2019; Piao et al., 2020). However, previous upscaled GPP datasets, as well as most LUE  
84 models such as the MODIS GPP product, have failed to consider the direct  $\text{CO}_2$  effects on leaf-  
85 level biochemical processes (Jung et al., 2020; Zheng et al., 2020). Consequently, these products  
86 likely underestimated the long-term trend of global GPP, leading to large discrepancies when  
87 compared to process-based models, which typically consider leaf-level  $\text{CO}_2$  effects (Anav et al.,  
88 2015; De Kauwe et al., 2016; O'Sullivan et al., 2020). Notably, recent improvements in LUE models  
89 have included the  $\text{CO}_2$  response and show improved long-term changes in GPP globally (Zheng et  
90 al., 2020), yet, this important mechanism is still missing in GPP products upscaled from *in situ* eddy  
91 covariance flux measurements.

92 To improve the quantification of GPP spatial and temporal dynamics and provide a robust  
93 representation of long-term dynamics in global photosynthesis, we developed the CEDAR-GPP<sup>1</sup>  
94 data product. CEDAR-GPP was upscaled from global eddy covariance carbon flux measurements  
95 using machine learning along with a broad range of multi-source satellite observations and climate  
96 variables. In addition to incorporating direct  $\text{CO}_2$  fertilization effects on photosynthesis, we also

---

<sup>1</sup> CEDAR stands for upsCaling Ecosystem Dynamics with ARTificial intelligence



97 account for indirect effects via greenness indicators and include novel satellite datasets such as solar-  
98 induced fluorescence (SIF), Land Surface Temperature (LST) and soil moisture to explain variability  
99 under environmental stresses. We provide monthly GPP estimations and associated uncertainties at  
100 0.05° resolution derived from ten model setups. These setups differ by the temporal range  
101 depending on satellite data availability, the method for incorporating the direct CO<sub>2</sub> fertilization  
102 effects, and the partitioning approach used to derive GPP from eddy covariance measurements.  
103 Short-term model setups were primarily based on data derived from MODIS satellites generating  
104 GPP estimates from 2001 to 2020, while long-term estimates spanned 1982 to 2020 using combined  
105 Advanced Very High Resolution Radiometer (AVHRR) and MODIS data. We used two approaches  
106 to incorporate the direct CO<sub>2</sub> fertilization effects, including direct prescription with eco-evolutionary  
107 theory and machine learning inference from the eddy-covariance data. Additionally, we provided a  
108 baseline configuration that did not incorporate the direct CO<sub>2</sub> effects. Uncertainties in GPP  
109 estimation were quantified using bootstrapped model ensembles. We evaluated the machine learning  
110 models' skills in predicting monthly GPP, seasonality, interannual variability, and trend against eddy  
111 covariance measurements, and compared the CEDAR-GPP spatial and temporal variability to  
112 existing satellite-based GPP estimates.

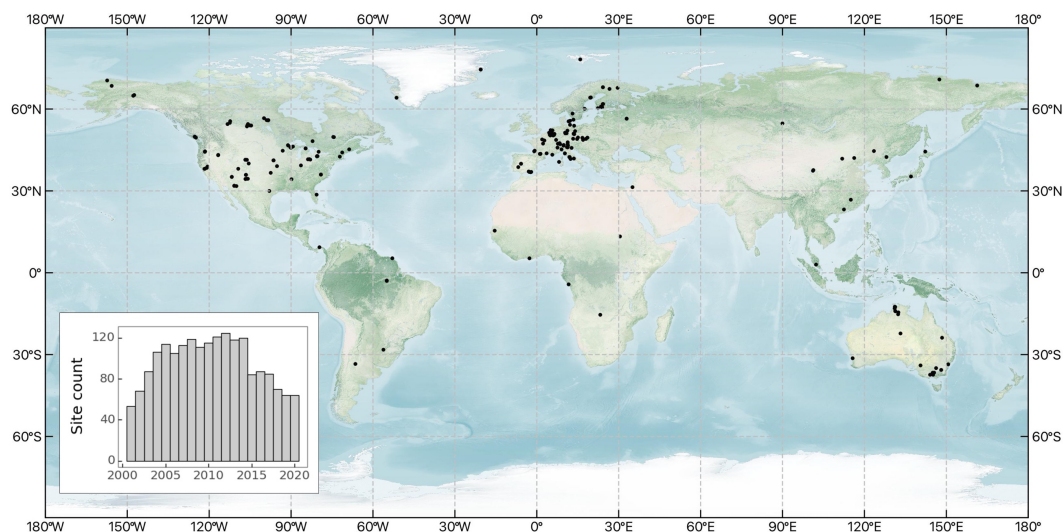
## 113 **2. Data and Methods**

### 114 **2.1 Eddy covariance data**

115 We obtained monthly eddy covariance GPP measurements from 2001 to 2020 from the  
116 FLUXNET2015 (Pastorello et al., 2020), AmeriFlux FLUXNET  
117 (<https://ameriflux.lbl.gov/data/flux-data-products/>), and ICOS Warm Winter 2020 (Warm Winter  
118 2020 Team and ICOS Ecosystem Thematic Centre., 2022) datasets. All data were processed with the  
119 ONEFLUX pipeline (Pastorello et al., 2020). Following previous upscaling efforts (Tramontana et  
120 al., 2016), we selected monthly GPP data with at least 80% of high-quality hourly or half-hourly data  
121 for temporal aggregation. We further excluded large negative GPP values, setting a cutoff of -1 gCm<sup>-2</sup>  
122 d<sup>-1</sup>. We utilized GPP estimates from both the night-time (GPP\_REF\_NT\_VUT) and day-time  
123 (GPP\_REF\_DT\_VUT) partitioning approaches. We classified flux tower sites according to the C3  
124 and C4 plant categories reported in metadata and related publications when available and used a C4  
125 plant percentage map (Still et al., 2003) otherwise. Our analysis encompassed 233 sites,



126 predominately located in North America, Western Europe, and Australia (Figure 1). In total, our  
 127 dataset included roughly 18000 site-months.



128

129 Figure 1. Global distribution of eddy covariance sites used to generate the CEDAR-  
 130 GPP product. The inset displays the annual count of sites. The base map was obtained  
 131 from the NASA Earth Observatory map by Joshua Stevens using data from NASA's  
 132 MODIS Land Cover, the Shuttle Radar Topography Mission (SRTM), the General  
 133 Bathymetric Chart of the Oceans (GEBCO), and Natural Earth boundaries.

## 134 2.2 Global input datasets

135 We compiled an extensive set of covariates from gridded climate reanalysis data, multi-source  
 136 satellite datasets including optical, thermal, and microwave observations, as well as categorical  
 137 information on land cover, climate zone, and C3/C4 classification. The datasets that we compiled  
 138 offer comprehensive information about GPP dynamics and its responses to climatic variabilities and  
 139 stresses. Table 1 lists the datasets and associated variables used to generate CEDAR-GPP.

140 Table 1. Datasets and input variables used to generate the CEDAR GPP product. For a list of  
 141 selected variables used in different model setups, please refer to Table S1.

Category	Dataset	Temporal coverage	Spatial resolution	Temporal resolution	Variables	Reference
Climate	ERA5-Land Monthly Averaged data	1950 – present	0.1°	Monthly	Air temperature; vapor pressure deficit, Precipitation,	(Sabater, 2019)



					Air and skin temperature, surface downwelling solar radiation, Potential evaporation	
	ESRA Global Monitoring Laboratory Atmospheric Carbon Dioxide	1976 – present	-	Monthly	Atmospheric CO <sub>2</sub> concentration averaged from Mauna Loa, Hawaii, US and South Pole, Antarctica	(Thoning et al., 2021)
Satellite-based datasets	MODIS Nadir BRDF-adjusted reflectance (MCD43C4v006)	2000 – present	0.05°	Daily	Surface reflectance b1 – b7, Vegetation indices (NIRv, NDVI, kNDVI, EVI, GCI, NDWI), percent snow	(Schaaf and Wang, 2015)
	MODIS Terra and Aqua LAI/fPAR (MCD15A3H, MOD15A2H, v006)	2000 – present	500m	4-day, 8-day	LAI, fPAR	(Myneni et al., 2015a, b)
	MODIS Terra and Aqua LST (MYD11A1, MOD11A1, v006)	2000 – present	1 km	Daily	Daytime LST Nighttime LST	(Wan et al., 2015b, a)
	BESS_Rad	2000 – 2020	0.05°	Daily	PAR, diffuse PAR, downwelling solar radiation	(Ryu et al., 2018)
	Continuous-SIF (from OCO-2 and MODIS)	2000 – 2020	0.05°	4-day	all-sky daily average SIF	(Zhang, 2021)
	ESA CCI Soil Moisture Combined Passive and Active (v06.1)	1979 – 2021	0.25°	Daily	Surface soil moisture	(Gruber et al., 2019)
	GIMMS LAI4g	1982 – 2021	0.0833°	Half-month	LAI	(Cao et al., 2023)
	GIMMS NDVI4g	1982 – 2021	0.0833 °	Half-month	NDVI	(Li et al., 2023)
	Static categorical datasets	MODIS Land Cover (MCD12Q1v006)	Average status used between 2001 and 2020	500m	-	Plant function types
	Koppen-Geiger Climate Classification	present	1 km	-	Koppen-Geiger climate classes	(Beck et al., 2018)



	C4 percentage map	present	1°	-	Percentage of C4 plants	(Still et al., 2003, 2009)
--	-------------------	---------	----	---	-------------------------	----------------------------

142

### 143 2.2.1 Climate variables

144 We obtained air temperature, vapor pressure deficit, precipitation, potential  
145 evapotranspiration, and skin temperature from the EAR5-Land reanalysis dataset (Sabater, 2019)  
146 (Table 1; Table S1). We applied a three-month lag to precipitation, to reflect the memory of soil  
147 moisture and represent the root zone water availability. Averaged monthly atmospheric CO<sub>2</sub>  
148 concentrations were calculated as an average of records from the Mauna Loa Observatory and South  
149 Pole Observation stations, retrieved from NOAA's Earth System Research Laboratory (Thoning et  
150 al., 2021).

### 151 2.2.2 Satellite datasets

152 We assembled a broad collection of satellite-based observations of vegetation greenness and  
153 structure, LST, solar radiation, solar-induced fluorescence (SIF), and soil moisture (Table 1, Table  
154 S1).

155 We used three MODIS version 6 products: surface reflectance, LAI/fAPAR, and LST.  
156 Surface reflectance from optical to infrared bands (band 1 to 7) was sourced from the MODIS  
157 Nadir BRDF-adjusted reflectance (NBAR) daily dataset (MCD43C4) (Schaaf and Wang, 2015).  
158 From these data, we derived vegetation indexes, including NIRv (Badgley et al., 2019), kNDVI  
159 (Camps-Valls et al., 2021), NDVI, Enhanced Vegetation Index (EVI), Normalized Difference Water  
160 Index (NDWI) (Gao, 1996), and the green chlorophyll index (CIgreen) (Gitelson, 2003). We also  
161 used snow percentages from the NBAR dataset. We used the 4-day LAI and fPAR composite  
162 derived from Terra and Aqua satellites (MCD15A3H) (Myneni et al., 2015a; Yan et al., 2016a, b)  
163 from July 2002 onwards and the MODIS 8-day LAI and fPAR dataset from Terra only  
164 (MOD15A2H) prior to July 2002 (Myneni et al., 2015b). We used day-time and night-time LST from  
165 the Aqua satellite (MYD11A1) (Wan et al., 2015b), with the Terra-based LST product (MOD11A1)  
166 used after July 2002 (Wan et al., 2015a). Terra LST was bias-corrected with the differences in the  
167 mean seasonal cycles between Aqua and Terra following Walther et al. (2022).

168 We used the PKU GIMMS NDVI4g dataset (Li et al., 2023) and PKU GIMMS LAI4g (Cao  
169 et al., 2023) datasets available from 1982 to 2020. PKU GIMMS NDVI4g is a harmonized time  
170 series that includes AVHRR-based NDVI from 1982 to 2003 (with biases and corrections mitigated





171 through inter-calibration with Landsat surface reflectance images) and MODIS NDVI from 2004  
172 onward. PKU GIMMS LAI4g consisted of AVHRR-based LAI from 1982 to 2003 (generated using  
173 machine learning models trained with Landsat-based LAI data and NDVI4g) and MODIS BNU  
174 LAI from 2004 onwards (Yuan et al., 2011).

175 We utilized photosynthetically active radiation (PAR), diffusive PAR, and shortwave  
176 downwelling radiation from the BESS\_Rad dataset (Ryu et al., 2018). We obtained the continuous-  
177 SIF (CSIF) dataset (Zhang et al., 2018; Zhang, 2021) produced by a machine learning algorithm  
178 trained using OCO-2 SIF observations and MODIS surface reflectance. We used surface soil  
179 moisture from the ESA CCI soil moisture combined passive and active product (version 6.1)  
180 (Dorigo et al., 2017; Gruber et al., 2019).

#### 181 2.2.3 Other categorical datasets

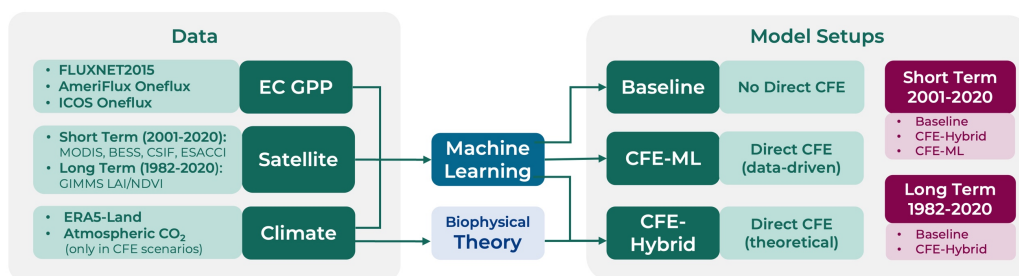
182 We used plant functional type (PFT) information derived from the MODIS Land Cover  
183 product (MCD12Q1) (Friedl and Sulla-Menashe, 2019). We followed the International Geosphere-  
184 Biosphere Program classification scheme but merged several similar categories to maximize the  
185 amount of eddy covariance sites/observations available for each category. Closed shrublands and  
186 open shrublands are combined into a shrubland category. Woody savannas and savannas are  
187 combined into savannas. We generated a static PFT map by taking the mode of the MODIS land  
188 cover time series between 2001 – 2020 at each pixel to mitigate uncertainties from misclassification  
189 in the MODIS dataset. Nevertheless, changes in vegetation structure induced by land use and land  
190 cover change are reflected in the dynamics surface reflectance and LAI/fAPAR datasets we used.  
191 We used the Koppen-Geiger main climate groups (tropical, arid, temperate, cold, and polar) (Beck et  
192 al., 2018). We also utilized a C4 plant percentage map to account for different photosynthetic  
193 pathways when incorporating CO<sub>2</sub> fertilization (Still et al., 2003, 2009).

#### 194 2.2.4 Data preprocessing

195 We implemented a three-step preprocessing strategy for the satellite datasets: 1) quality  
196 control, 2) gap-filling, and 3) spatial and temporal aggregation. In the first step, we selected high-  
197 quality data based on the quality control flags of the satellite products when available. For the  
198 MODIS NBAR dataset (MCD43C3), we used data with 75% or more high-resolution NBAR pixels  
199 retrieved with full inversions for each band. For MODIS LST, we selected the best quality data from  
200 the quality control bitmask as well as data where retrieved values had an average emissivity error of  
201 no more than 0.02. For MODIS LAI/fAPAR, we used retrievals from the main algorithm with or



202 without saturation. We used all available data in ESA-CCI soil moisture due to the presence of  
 203 substantial data gaps. In the gap-filling step, missing values in satellite datasets were temporally filled  
 204 at the native temporal resolution, following a two-step protocol adapted from Walther et al (2021).  
 205 Short temporal gaps were first filled with medians from a moving window, and the remaining gaps  
 206 were filled with the mean seasonal cycle. For datasets with a high temporal resolution, including  
 207 MODIS NBAR (daily), LAI/fPAR (4-day), BESS (4-day), CSIF (4-day), ESA-CCI (daily), temporal  
 208 gaps no longer than 5 days (8 days for 4-day resolution products) were filled with medians of 15-day  
 209 moving windows in the first step. An exception is MODIS LST (daily), for which we used a shorter  
 210 moving window of 9 days due to rapid changes in surface temperature. GIMMS LAI4g and  
 211 NDVI4g data were only filled with mean seasonal cycle due to their low temporal resolution (bi-  
 212 monthly). In the last processing step, all the datasets were aggregated to a monthly time step and  
 213 0.05-degree spatial resolution.



214

215 Figure 2. Schematic overview of the CEDAR-GPP model setups.

## 216 2.3 Machine learning upscaling

### 217 2.3.1 CEDAR-GPP model setups

218 We trained machine learning models with eddy covariance GPP measurements as targets and  
 219 climate/satellite variables as input features. We created ten model setups to produce different global  
 220 monthly GPP estimates (Figure 2; Table 2). The model setups were characterized by the temporal  
 221 range depending on input data availability, the configuration of CO<sub>2</sub> fertilization effects, and the  
 222 partitioning approach used to derive the GPP from eddy covariance measurements.

223 The short-term (ST) model configuration produced GPP from 2001 to 2020, and the long-  
 224 term (LT) configuration spanned 1982 to 2020. Each temporal configuration uses a different set of  
 225 input variables depending on their availability. Inputs for the short-term configuration included  
 226 MODIS, CSIF, BESS PAR, ESA-CCI soil moisture, ERA5-Land, as well as PFT and Koppen



227 Climate zone as categorical variables with one-hot encoding. The long-term used GIMMS NDVI4g  
 228 and LAI4g data, ERA5-land, PFT and Koppen climate. ESA CCI soil moisture datasets were  
 229 excluded from the long-term model setups due to concerns about the product quality in the early  
 230 years when the number and quality of microwave satellite data were limited (Dorigo et al., 2015). A  
 231 detailed list of input features for each setup is provided in Table S1.

232 Regarding the direct (leaf-level) CO<sub>2</sub> fertilization effects (CFE), we established a “Baseline”  
 233 configuration that did not incorporate these effects, a “CFE-Hybrid” configuration that  
 234 incorporated the effects via eco-evolutionary theory, and a “CFE-ML” configuration that inferred  
 235 the direct effects from eddy covariance data using machine learning. Detailed information about  
 236 these approaches is provided in Sec. 2.4.2. Furthermore, separate models were trained for GPP  
 237 target variables from the night-time (NT) and daytime (DT) partitioning approaches.

238 Table 2 lists the characteristics of ten model setups. Note that due to the limited availability of  
 239 eddy covariance observations before 2001, we did not apply the CFE-ML approach to the long-term  
 240 setups, as the machine learning inferred CO<sub>2</sub> fertilization effects cannot be robustly extrapolated  
 241 back to 1982.

242 Table 2. Specifications of the CEDAR-GPP model setups.

Model Setup Name	Temporal range	Direct CO <sub>2</sub> Fertilization Effects		GPP Partitioning Method
		Configuration	Method	
ST_Baseline_NT	Short-term (ST) 2001 – 2020	Baseline	Not incorporated	Night-time (NT)
ST_Baseline_DT				Day-time (DT)
ST_CFE-Hybrid_NT		CFE-Hybrid	Theoretical	NT
ST_CFE-Hybrid_DT				DT
ST_CFE-ML_NT		CFE-ML	Data-driven	NT
ST_CFE-ML_DT				DT
LT_Baseline_NT	Long-term (LT) 1982 – 2020	Baseline	Not incorporated	NT
LT_Baseline_DT				DT
LT_CFE-Hybrid_NT		CFE-Hybrid	Theoretical	NT
LT_CFE-Hybrid_DT				DT

243

### 244 2.3.2 CO<sub>2</sub> fertilization effect

245 We established three configurations considering the direct CO<sub>2</sub> fertilization effects on  
 246 photosynthesis. In the baseline configuration, we trained machine learning models with eddy  
 247 covariance GPP measurements, input climate and satellite features, but excluding CO<sub>2</sub>  
 248 concentration. As such, the models only include indirect CO<sub>2</sub> effects from the satellite-based proxies  
 249 of vegetation greenness and structure and do not consider the direct effect of CO<sub>2</sub> on light use



250 efficiency. Our baseline model is therefore directly comparable to other satellite-derived GPP  
251 products that only account for indirect CO<sub>2</sub> effects (Jung et al., 2020; Joiner and Yoshida, 2020).

252 In the CFE-ML configuration, we added monthly CO<sub>2</sub> concentration into the feature set in  
253 addition to those incorporated in the baseline models. Thus, models inferred the functional  
254 relationship between GPP and CO<sub>2</sub> from the eddy covariance data, encompassing both CO<sub>2</sub>  
255 fertilization pathways – direct effects on LUE and indirect effects from the satellite-based proxies of  
256 vegetation greenness and structure.

257 In the CFE-Hybrid configuration, we applied biophysical theory to estimate the response of  
258 LUE to elevated CO<sub>2</sub>. First, we estimated a reference GPP, where LUE was not affected by any  
259 increase in atmospheric CO<sub>2</sub>, by applying the CFE-ML model with a constant atmospheric CO<sub>2</sub>  
260 concentration equal to the 2001 level while keeping all other variables temporally dynamic. Then, the  
261 impacts of CO<sub>2</sub> on LUE were prescribed onto the reference GPP estimates using a theoretical CO<sub>2</sub>  
262 sensitivity function of LUE according to eco-evolutionary theories (Appendix A). The theoretical  
263 CO<sub>2</sub> sensitivity function represents a CO<sub>2</sub> sensitivity that is equivalent to that of the electron-  
264 transport-limited (light-limited) photosynthetic rate. When light is limited, elevated CO<sub>2</sub> suppresses  
265 photorespiration leading to increased photosynthesis at a lower rate than when photosynthesis is  
266 limited by CO<sub>2</sub> (Lloyd and Farquhar, 1996; Smith and Keenan, 2020). Thus, the CFE-Hybrid  
267 scenario provides a conservative estimation of the direct CO<sub>2</sub> effects on LUE. Note that the  
268 theoretical sensitivity function describes the fractional change in LUE due to direct CO<sub>2</sub> effects  
269 relative to a reference period (i.e. 2001). Therefore, we used the CFE-ML model to establish this  
270 reference GPP by fixing the CO<sub>2</sub> effects to the 2001 level, rather than simply using the GPP from  
271 the Baseline model in which the direct CO<sub>2</sub> effects were not represented.

272 For both CFE-ML and CFE-Hybrid scenarios, we made another conservative assumption that  
273 C4 plants do not benefit from elevated CO<sub>2</sub>, despite potential increases in photosynthesis during  
274 water-limited conditions due to enhanced WUE. Data from flux tower sites dominated by C4 plants  
275 were removed from our training set, so the machine learning models inferred CO<sub>2</sub> fertilization only  
276 from flux tower sites dominated by C3 plants. When applying models globally, we assumed the  
277 reference GPP values (with constant atmospheric CO<sub>2</sub> concentration equal to the 2001 level) to  
278 represent C4 plants, and GPP estimates from CFE-ML or CFE-Hybrid models were applied in  
279 proportion to the percentage of C3 plants in a grid cell.



### 280 2.3.3 Machine learning model training and validation

281 We employed the state-of-the-art XGBoost machine learning model, known for its high  
282 accuracy in regression problems across various domains, including environmental and ecological  
283 predictions (Chen and Guestrin, 2016; Kang et al., 2020; Berdugo et al., 2022). XGBoost is a  
284 scalable and parallelized implementation of the gradient boosting technique that iteratively trains an  
285 ensemble of decision trees, with each iteration targeting to minimize the residuals from the last  
286 iteration. A notable merit of XGBoost is its ability to make prediction in the presence of missing  
287 values, a common issue in remote sensing datasets.

288 We used five-fold cross-validation for model evaluation. Training data was randomly split into  
289 five groups (folds), with each fold held out for testing while the rest four folds were used for model  
290 training. We imposed two restrictions on fold splitting; each flux site was entirely assigned to a fold  
291 to test model performance over unseen locations; the random sampling was stratified based on PFT  
292 to ensure coverage of the full range of PFTs in both training and testing. We also used a nested-  
293 cross-validation strategy, during which we performed a randomized search of hyperparameters using  
294 three-fold cross-validation within the training set. The nested-cross-validation was aimed to reduce  
295 the risk of overfitting and improve the robustness of the evaluation.

296 We assessed the models' ability to capture the temporal and spatial characteristics of GPP,  
297 including monthly GPP, mean seasonal cycles, monthly anomalies, and cross-site variability. Model  
298 performance was assessed separately for each model setup (Table 2) and summarized by PFT and  
299 Koppen climate zone. Mean seasonal cycles were calculated as the mean monthly GPP over the site  
300 observation period, and monthly anomalies were the residuals of monthly GPP after subtracting  
301 mean seasonal cycles. Monthly GPP averaged over years for each site was used to assess cross-site  
302 variability. Goodness-of-fit metrics include RMSE, bias, and coefficient of determination ( $R^2$ ).

303 To evaluate the models' ability to capture long-term GPP trends, we aggregated the monthly  
304 GPP to annual values for sites with at least five years of observations following Chen et al. (2022).  
305 GPP anomalies were computed by subtracting the multi-year mean GPP from the annual GPP for  
306 each site. Anomalies were aggregated across sites to achieve a single multi-site GPP anomaly per  
307 year. We used the Sen slope and Mann-Kendall test to examine the GPP trends from 2002 to 2019,  
308 excluding 2001 and 2020, due to the limited number of available sites with more than five years of  
309 data.



#### 310 2.3.4 Product generation and uncertainty quantification

311 In the CEDAR-GPP product, we generated GPP estimates from each of the ten model  
312 setups, by applying the model to global gridded datasets within the corresponding temporal range  
313 (Table 2). GPP estimates were named after the corresponding model setups. We used bootstrapping  
314 to quantify estimate uncertainties. For each model setup, we generated 30 bootstrapped sample sets  
315 of eddy covariance data, which were then used to train an ensemble of 30 XGBoost models. The  
316 bootstrapping was performed at the site level, and each bootstrapped sample set contained around  
317 140 to 150 unique sites, 17000 to 19000 site months covering all PFTs. The relative PFT  
318 composition in the bootstrapped sample sites was consistent with the full dataset. The 30 models  
319 trained with bootstrapped samples generated an ensemble of 30 GPP values. We provided the  
320 ensemble GPP mean and used standard deviation to indicate uncertainties, for each of the ten model  
321 setups.

#### 322 2.4 Product inter-comparison

323 We compared the global spatial and temporal patterns of CEDAR-GPP with other major  
324 satellite-based GPP products, including three machine learning upscaled and two LUE-based  
325 datasets. We obtained two FLUXCOM products (Jung et al., 2020), the latest version of  
326 FLUXCOM-RS (FLUXCOM-RSv006) available from 2001 to 2020 based on remote sensing  
327 (MODIS collection 6) datasets only, as well as the FLUXCOM-RS+METEO ensemble available  
328 between 1979 to 2018 and based on the climatology of remote sensing observations and ERA5  
329 forcings (hereafter FLUXCOM-ERA5). We used FluxSat (Joiner and Yoshida, 2020), available from  
330 2001 to 2019, which is an upscaled dataset based on MODIS NBAR surface reflectance and PAR  
331 from Modern-Era Retrospective analysis for Research and Applications 2 (MERRA-2). Importantly,  
332 FluxSat does not incorporate climate forcings. We used the MODIS GPP product (MOD17)  
333 available since 2001, which was generated based on MODIS fAPAR and LUE as a function of air  
334 temperature and vapor pressure deficit but not atmospheric CO<sub>2</sub> concentration (Running et al.,  
335 2015). We also used the rEC-LUE products, available from 1982 to 2018 and based on a revised  
336 LUE model that incorporated the effect of atmospheric CO<sub>2</sub> concentration and the fraction of  
337 diffuse PAR on LUE (Zheng et al., 2020). All datasets were resampled to 0.1 ° spatial resolution, and  
338 a common mask for the vegetated land area was applied. We evaluated global mean annual GPP,  
339 mean seasonal cycle, interannual variability, and trend among different datasets, comparing them



340 over a common time period determined by their data availability. Global total GPP was computed  
 341 by scaling the global average GPP flux with the global land area (122.4 million km<sup>2</sup>) following Jung  
 342 et al. (2020). Mean seasonal cycle was defined as above (Sec. 2.3.3). We used the standard deviation  
 343 of annual GPP to indicate the magnitude of interannual variability, the Sen slope to indicate the  
 344 GPP annual trend, and the Mann-Kendall test for the statistical significance of trends.

### 345 3. Results

#### 346 3.1 Evaluation of model performance

##### 347 3.1.1 Overall performance

348 The short-term and long-term models explained approximately 74% and 68%, respectively, of  
 349 the variation in monthly GPP across global eddy covariance sites (Figure 3a). The long-term models  
 350 consistently yielded lower performance than the short-term models, likely due to differences in the  
 351 satellite remote sensing datasets used, as the short-term models benefited from richer information  
 352 from surface reflectance of individual bands, LST, CSIF, as well as soil moisture, while the long-  
 353 term model only exploited NDVI and LAI. The models with different CFE configurations and  
 354 target GPP variables (i.e. partitioning approaches) had similar performance in predicting monthly  
 355 GPP (Figure 3b, Table 3, Table S2). All models exhibited minimal bias of less than 0.15.

356 Model performance in terms of the different temporal and spatial characteristics of monthly  
 357 GPP was variable (Figure 3c-h). The models were most successful at predicting mean seasonal  
 358 cycles, with the short-term and long-term models explaining around 79% and 73% of the variability,  
 359 respectively (Figure 3c-d). The short-term and long-term models captured 67% and 56% ,  
 360 respectively, of the spatial variabilities in multi-year mean GPP across global sites (i.e., cross-site  
 361 variability) (Figure 3g-h). However, all models predicted monthly anomalies across the sites, with R<sup>2</sup>  
 362 values below 0.12 (Figure 3e-f). The CFE-ML and CFE-Hybrid models showed slightly higher  
 363 accuracy than the Baseline model across all temporal and spatial characteristics in NT setups.

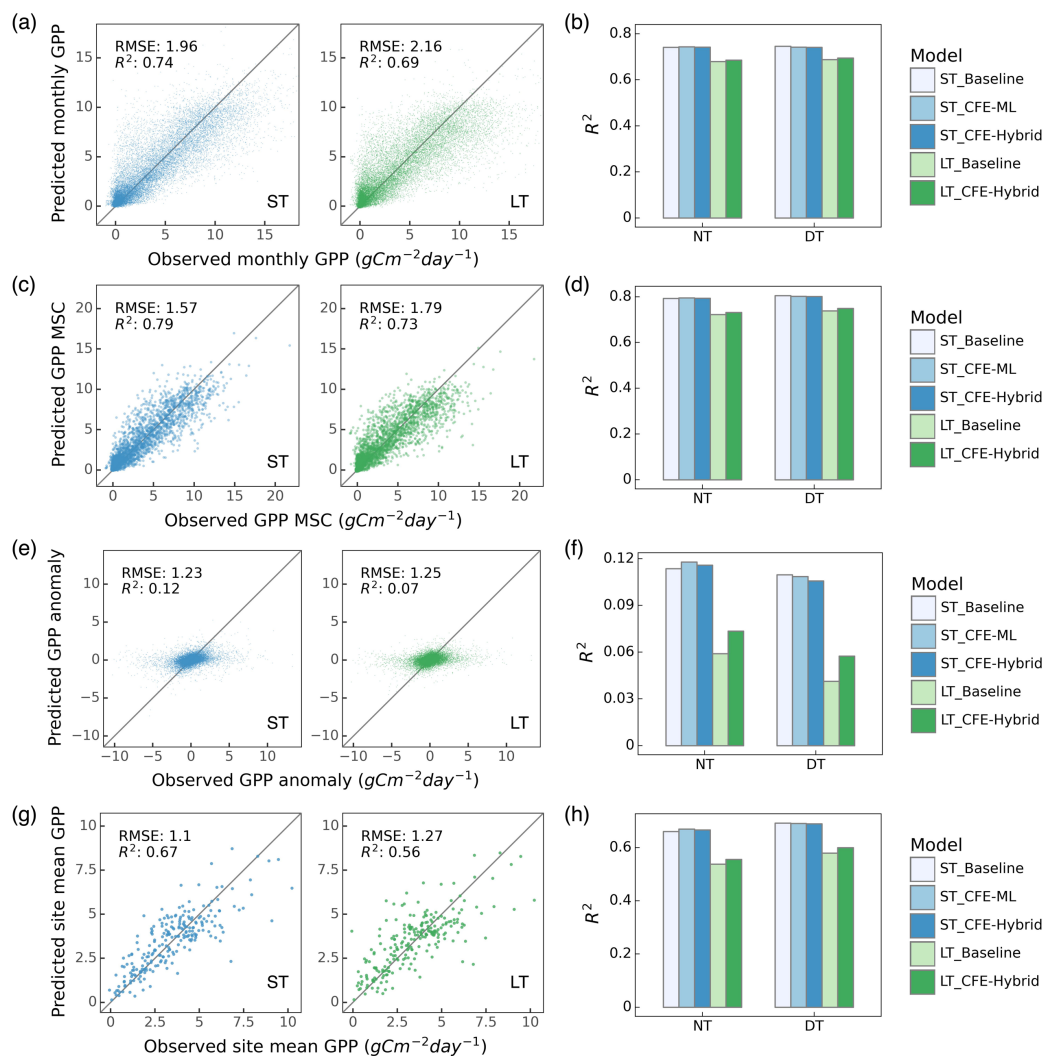
364 Table 3. Machine learning model performance for five CEDAR-GPP setups based on NT GPP  
 365 (Table 2). Results of DT setups can be found in Table S2.

Model Setup Name	Monthly			Mean seasonal cycles			Monthly anomalies			Cross-site		
	RMSE	Bias	R <sup>2</sup>	RMSE	Bias	R <sup>2</sup>	RMSE	Bias	R <sup>2</sup>	RMSE	Bias	R <sup>2</sup>
ST_Baseline_NT	1.96	-0.05	0.74	1.57	0.02	0.79	1.22	0.00	0.11	1.11	0.03	0.66



ST_CFE-ML_NT	1.95	-0.05	0.74	1.56	0.02	0.80	1.22	0.00	0.12	1.10	0.03	0.67
ST_CFE-Hybrid_NT	1.96	-0.05	0.74	1.57	0.03	0.79	1.23	0.00	0.12	1.10	0.04	0.67
LT_Baseline_NT	2.18	-0.10	0.68	1.82	0.01	0.72	1.26	0.00	0.06	1.29	0.03	0.54
LT_CFE-Hybrid_NT	2.16	-0.11	0.69	1.79	0.01	0.73	1.25	0.00	0.07	1.27	0.03	0.56

366



367

368

369

370

371

372

Figure 3. Machine learning model performance in predicting monthly GPP and its spatial and temporal variability. Scatter plots illustrated relationships between model predictions and observations for monthly GPP (a), mean seasonal cycles (MSC) (c), monthly anomaly (e), and cross-site variability (g) for ST\_CFE-Hybrid\_NT (left, blue) and LT\_CFE-Hybrid\_NT (right, green) models. Corresponding bar plots show the  $R^2$





373 values for all ten model setups in predicting monthly GPP (b), MSC (d), monthly  
374 anomaly (f), and cross-site variability (h).

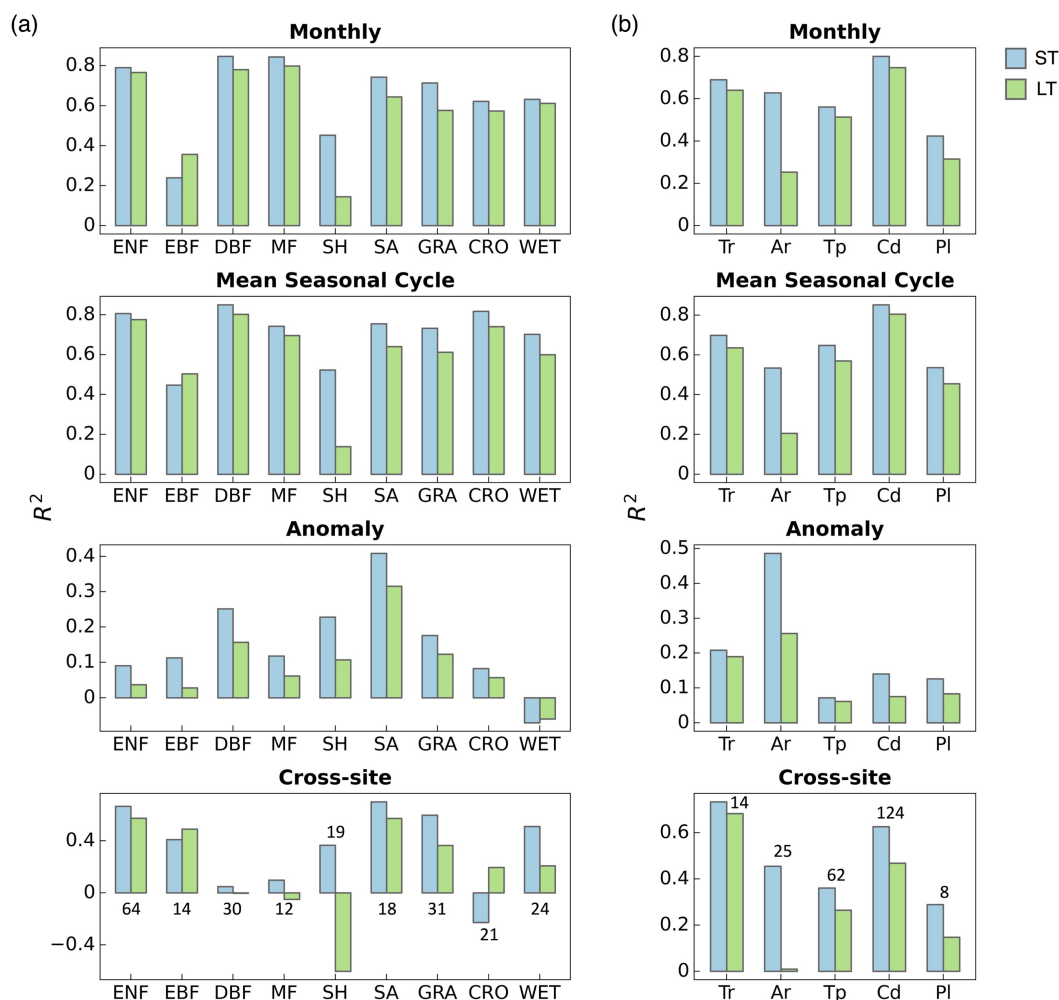
### 375 3.1.2 Performance by biome and climate zone

376 The predictive ability of our models varied across different PFTs and Koppen climate zones  
377 (Figure 4). Here we present results from the CFE-Hybrid LT and ST models based on NT  
378 partitioning and note that patterns for the other CFE configurations and the DT GPP were similar.

379 Model performance in terms of monthly GPP was the highest for deciduous broadleaf forests,  
380 mixed forests, and evergreen needleleaf forests, with  $R^2$  values above 0.78. Model accuracies were  
381 also high for savannas, and grasslands, followed by croplands and wetlands, with  $R^2$  values between  
382 0.57 and 0.74. Model accuracies were lowest in evergreen broadleaf forests and shrublands, with  $R^2$   
383 values as low as 0.14. Across climate zones, models achieved the highest accuracy in predicting  
384 monthly GPP in cold and tropical climate zones with  $R^2$  values between 0.64 and 0.80. The short-  
385 term models had the lowest performance in polar regions with an  $R^2$  value of around 0.42, and the  
386 long-term model had the lowest performance in arid regions with an  $R^2$  value of 0.25.

387 Model performance in terms of mean seasonal cycles across PFTs and climate zones followed  
388 patterns for monthly GPP, while disparities emerged for performance in terms of GPP anomaly and  
389 cross-site variability (Figure 4). The short-term model showed the highest predictive power in  
390 explaining monthly anomalies in arid regions with an  $R^2$  value of 0.49, where savanna and  
391 shrublands sites are primarily located. Model performance in all other climate zones was significantly  
392 lower, with  $R^2$  values below 0.2, and as low as 0.07 in temperate regions. Besides, the short-term  
393 model demonstrated good performance in capturing anomalies in deciduous broadleaf forests. The  
394 long-term model's relative performance between PFTs and climate zones was mostly consistent with  
395 that of the short-term model, with lower accuracy in shrublands when compared to the short-term  
396 model.

397 Models demonstrated the highest accuracy in predicting cross-site variability in savannas,  
398 grasslands, evergreen needleleaf forests, and evergreen broadleaf forests ( $R^2 > 0.36$ ) and the lowest  
399 accuracy in deciduous broadleaf forests, mixed forests, and croplands ( $R^2 < 0.20$ ). The short-term  
400 model additionally showed good performance in shrublands and wetlands ( $R^2 > 0.36$ ), whereas the  
401 long-term model failed to capture any variability for shrublands. In terms of climate zones, models  
402 were most successful at explaining the variabilities within tropical and cold climate zones ( $R^2 >$   
403 0.46), the short-term model was least successful across polar regions, with a  $R^2$  value of 0.29, and the  
404 long-term model had low performance for both polar and arid regions with  $R^2$  values below 0.15.



405

406

407

408

409

410

411

Figure 4. Performance of the ST\_Hybrid\_NT (blue) and LT\_Hybrid\_NT (green) models on GPP spatiotemporal estimation by plant functional types (a) and climate zones (b). The cross-site panels included the number of sites within each category. ENF: evergreen needleleaf forest, EBF: evergreen broadleaf forest, DBF: deciduous broadleaf forest, MF: mixed forest, SH: shrubland, SA: savanna, GRA: grassland, CRO: cropland, WET: wetland. Tr: tropical, Ar: arid, Tp: temperate, Cd: cold, PI: polar.

### 412 3.1.3 Prediction of long-term trends

413

414

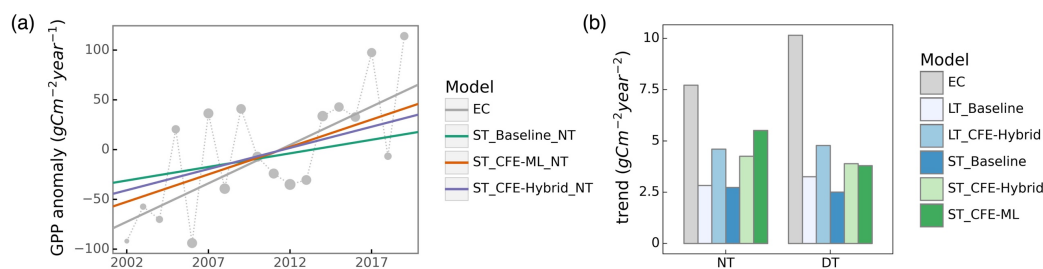
415

Eddy covariance derived GPP presented a substantial increasing trend across flux sites between 2002 and 2019 (Figure 5a). The observed GPP from the night-time partitioning approach indicated an overall trend of  $7.7 \text{ gCm}^{-2}\text{year}^{-2}$ . In contrast, the ST\_Baseline\_NT model predicted a



416 more modest trend of  $2.7 \text{ gCm}^{-2}\text{year}^{-2}$ , primarily reflecting the indirect  $\text{CO}_2$  effect manifested  
417 through the growth of LAI. Both the ST\_CFE-ML\_NT and ST\_CFE-hybrid\_NT models predicted  
418 much higher trends of  $5.5$  and  $4.3 \text{ gCm}^{-2}\text{year}^{-2}$  respectively, aligning more closely to eddy covariance  
419 observations.

420 The CFE-ML and CFE-hybrid models consistently outperformed the Baseline models in  
421 predicting GPP trends in global eddy covariance towers (Figure 6b) and all trends were statistically  
422 significant ( $p < 0.05$ ). Notably, we found a considerably higher trend in eddy covariance GPP  
423 measurements derived from the day-time versus night-time partitioning approach. The predicted  
424 trends of different model setups between the partitioning approaches were similar despite a smaller  
425 trend predicted by the ST\_CFE-ML\_DT model compared to the corresponding NT model (Figure  
426 6b).



427  
428 Figure 5. Comparison of observed and predicted GPP trends across eddy covariance  
429 flux towers. (a) Aggregated annual GPP anomaly from 2002 to 2019 and trend lines  
430 from eddy covariance (EC) measurements, and three CFE model setups (short-term,  
431 night-time partitioning). The size of grey circle markers is proportional to the number  
432 of sites. (b) Annual trends from eddy covariance measurements and ten CEDAR-GPP  
433 model setups.

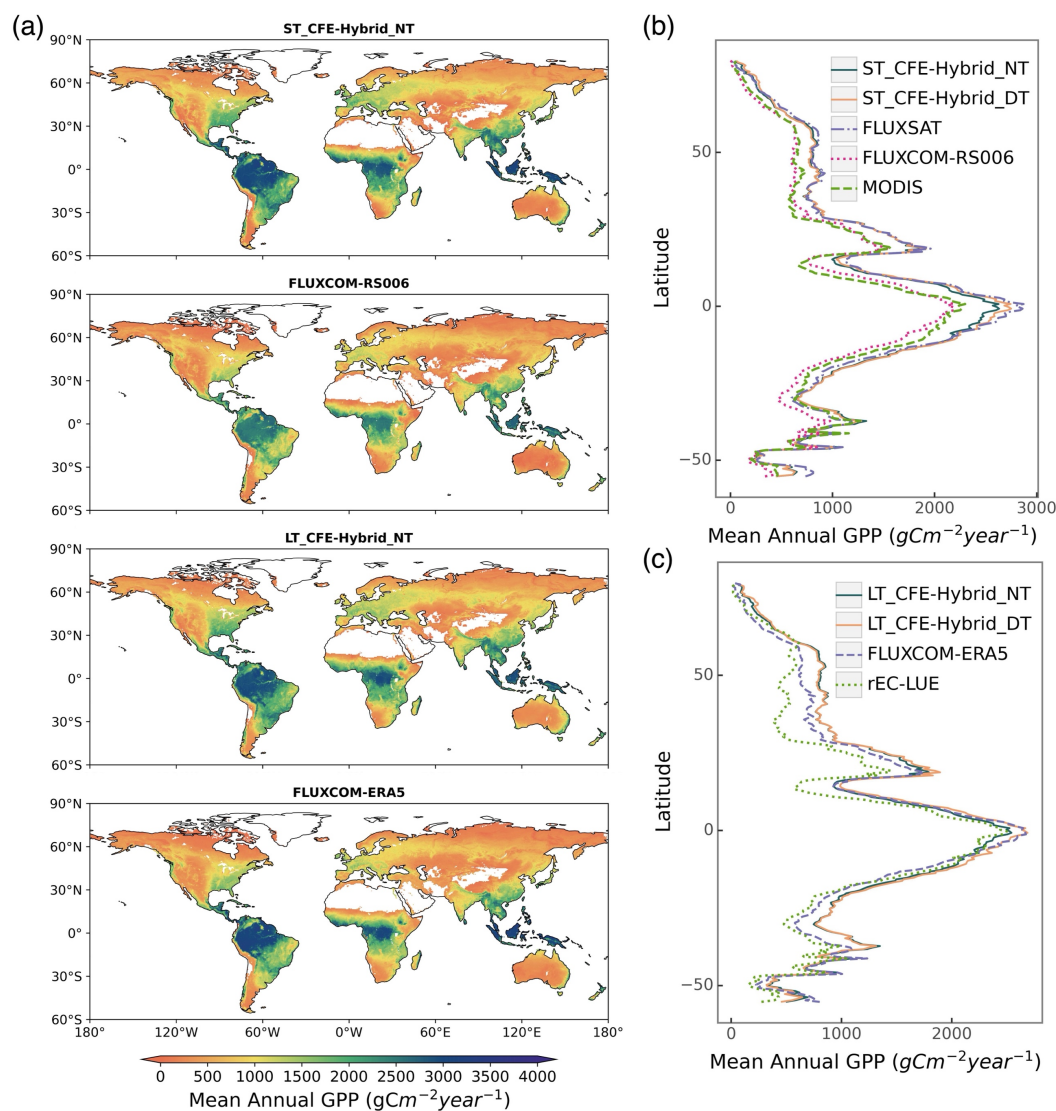
### 434 3.2 Evaluation of GPP spatial and temporal dynamics

435 We compared CEDAR-GPP estimates with other upscaled or LUE-based datasets regarding  
436 the mean annual GPP (Sect. 3.2.1), GPP seasonality (Sect. 3.2.2), interannual variability (Sect. 3.2.3),  
437 and annual trends (Sect. 3.2.4). CEDAR-GPP model setups generally showed similar patterns in  
438 mean annual GPP, seasonality, and interannual variability, therefore, in corresponding sections, we  
439 present the CFE-Hybrid model setups as representative examples for comparisons with other  
440 datasets, unless otherwise stated. Supplementary figures include comparisons involving CEDAR-  
441 GPP estimates from all model setups.



### 442 3.2.1 Mean annual GPP

443 Global patterns of mean annual GPP were generally consistent among CEDAR-GPP model  
444 setups, FLUXCOM, FLUXSAT, MODIS, and rEC-LUE, with few noticeable regional differences  
445 (Figure 6, Figure S1). Differences among CEDAR-GPP model setups were minimal and only  
446 evident between the NT and DT setups in the tropics (Figure 6b-c, Figure S1). CEDAR-GPP short-  
447 term datasets showed highest consistency with FLUXSAT in terms of mean annual GPP  
448 magnitudes (2001 – 2018) and latitudinal variations, although FLUXSAT presented slightly higher  
449 GPP values in the tropics compared to CEDAR-GPP (Figure 6b). Mean annual GPP magnitude for  
450 FLUXCOM-RS006 and MODIS was lower globally than CEDAR-GPP and FLUXSAT, with the  
451 most pronounced differences observed in the tropical areas. Among the long-term datasets  
452 (CEDAR-GPP LT, FLUXCOM-ERA5, and rEC-LUE), mean annual GPP (1982 – 2018) exhibited  
453 greater disparities in the northern mid-latitudes than in the tropics and southern hemisphere (Figure  
454 6c). CEDAR-GPP aligned more closely with FLUXCOM-ERA5 than with rEC-LUE, with the latter  
455 showing lower annual mean GPP globally, particularly between 20°N to 50° N.



456

457

458

459

460

461

462

463

464

465

466

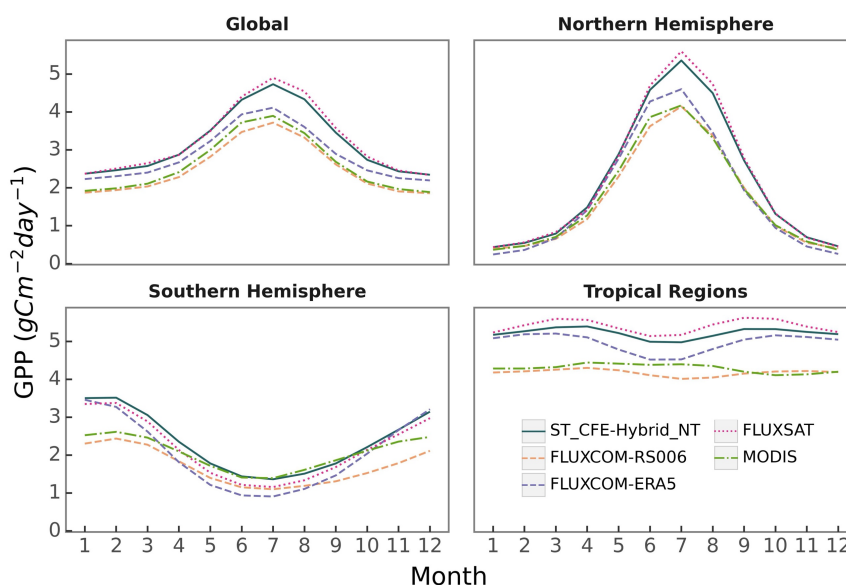
Figure 6. Global distributions of mean annual GPP from CEDAR-GPP and other machine learning upscaled and LUE-based reference datasets. (a) Global patterns of mean annual GPP from two short-term datasets including ST\_CFE-Hybrid\_NT, and FLUXCOM-RS006, and two long-term datasets including LT\_CFE-Hybrid\_NT, and FLUXCOM-ERA5. (b) Latitudinal distributions of mean annual GPP from short-term datasets (ST\_CFE-Hybrid\_NT, ST\_CFE-Hybrid\_DT, FLUXSAT, FLUXCOM-RS006, and MODIS). (c) Latitudinal distributions of mean annual GPP from long-term datasets (LT\_CFE-Hybrid\_NT, LT\_CFE-Hybrid\_DT, FLUXCOM-ERA5, and rEC-LUE). Mean annual GPP was computed between 2001 and 2018 for short-term datasets and between 1982 and 2018 for long-term datasets.



### 467 3.2.2 Seasonal variability

468 CEDAR-GPP and other machine learning upscaled or LUE-based GPP datasets agreed on  
469 seasonal variabilities (average between 2001 and 2018) at the global scale, characterized by a peak in  
470 GPP in July and a nadir between December and January (Figure 7). At the global scale, CEDAR-  
471 GPP was most closely aligned with FLUXSAT in GPP seasonal magnitude and amplitude, while  
472 both FLUXCOM and MODIS displayed a relatively less pronounced magnitude.

473 In the northern hemisphere (20°N - 90°N), all GPP datasets agreed on seasonal GPP  
474 variation, despite variances in the magnitude of peak GPP. In the southern hemisphere (20°S -  
475 60°S), all datasets exhibited their lowest GPP during June and July, and highest GPP from  
476 December to January. However, the seasonal amplitude of GPP was greatest for FLUXCOM-  
477 ERA5, followed by CEDAR-GPP and FLUXSAT, and substantially smaller for FLUXCOM-RS006  
478 and MODIS GPP. In the tropics (20°N - 20°S), differences between datasets were the strongest,  
479 where seasonal variation is not as prominent compared to other regions. CEDAR-GPP, FLUXSAT,  
480 and FLUXCOM-ERA5 each showed two GPP peaks, occurring in March-April and September-  
481 October. Although FLUXCOM-RS006 had a similar seasonal pattern, its GPP magnitude was  
482 markedly smaller. Interestingly, MODIS showed an inverse season pattern with a small peak from  
483 June to August.



484  
485  
486

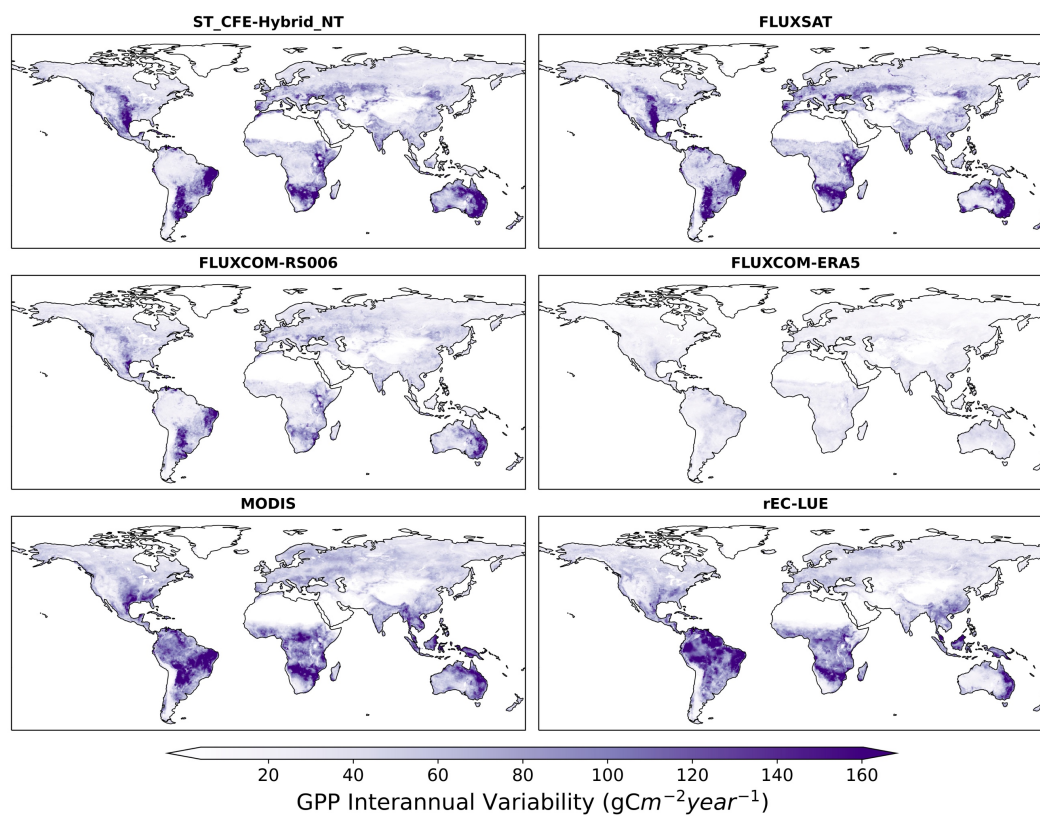
Figure 7. Comparison of GPP mean seasonal cycle between different datasets on a global scale, specifically within the Northern Hemisphere (20°N - 90°N), Southern



487 Hemisphere (20°S - 60°S), and Tropical regions (20°N - 20°S). Monthly means were  
488 averaged from 2001 to 2018 for all datasets.

### 489 3.2.3 Interannual variability

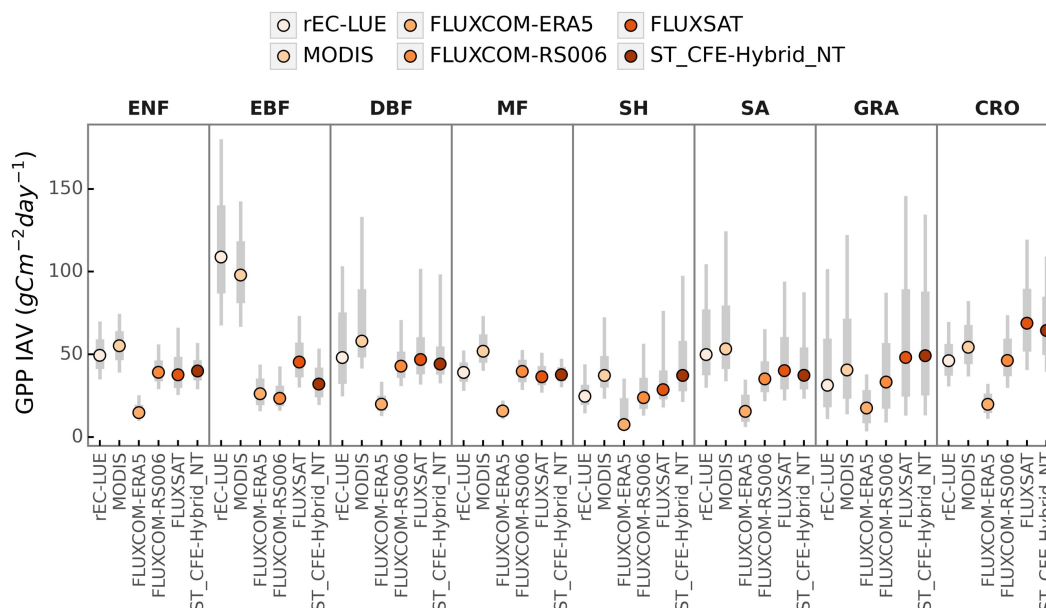
490 We found distinct spatial patterns in GPP interannual variability between upscaled and LUE-  
491 based datasets and a high level of agreement within each category, with the exception of  
492 FLUXCOM-ERA5, which showed minimal interannual variability globally (Figure 8). All datasets  
493 agreed on the presence of GPP interannual variability hotspots in eastern and southern South  
494 America, central North America, southern Africa, and western Australia. These hotspots primarily  
495 corresponded to arid and semi-arid areas characterized by grasslands, shrubs, and croplands (Figure  
496 9). CEDAR-GPP was highly consistent with FLUXSAT, and both datasets also displayed relatively  
497 high interannual variability in the dry subhumid areas of Europe, predominately covered by  
498 croplands. FLUXCOM-RS006 mirrored the relative spatial patterns of CEDAR-GPP and  
499 FLUXSAT, albeit at lower magnitudes. The LUE-based datasets (MODIS and rEC-LUE) predicted  
500 a much higher interannual variability than the upscaled datasets in the tropical areas, particularly in  
501 evergreen broadleaf forests and woody savannas (Figure 8, Figure 9). These datasets also depicted  
502 slightly higher interannual variability for other types of forests, including evergreen needleleaf forests  
503 and deciduous broadleaf forests, compared to the upscaled datasets.



504  
505  
506  
507

Figure 8. Spatial patterns of GPP interannual variability extracted over 2001 to 2018 for CEDAR-GPP (ST\_CFE-Hybrid\_NT), FLUXSAT, FLUXCOM-RS006, MODIS, FLUXCOM-ERA5, and rEC-LUE.





508

509 Figure 9. Comparison of GPP interannual variability (IAV) across global datasets by  
 510 PFT. Colored dots represent the median IAV, thicker gray bars indicate the 25% to  
 511 75% percentiles of IAV distributions, and thinner grey bars show the 10% to 90%  
 512 percentiles.

### 513 3.2.4 Trends

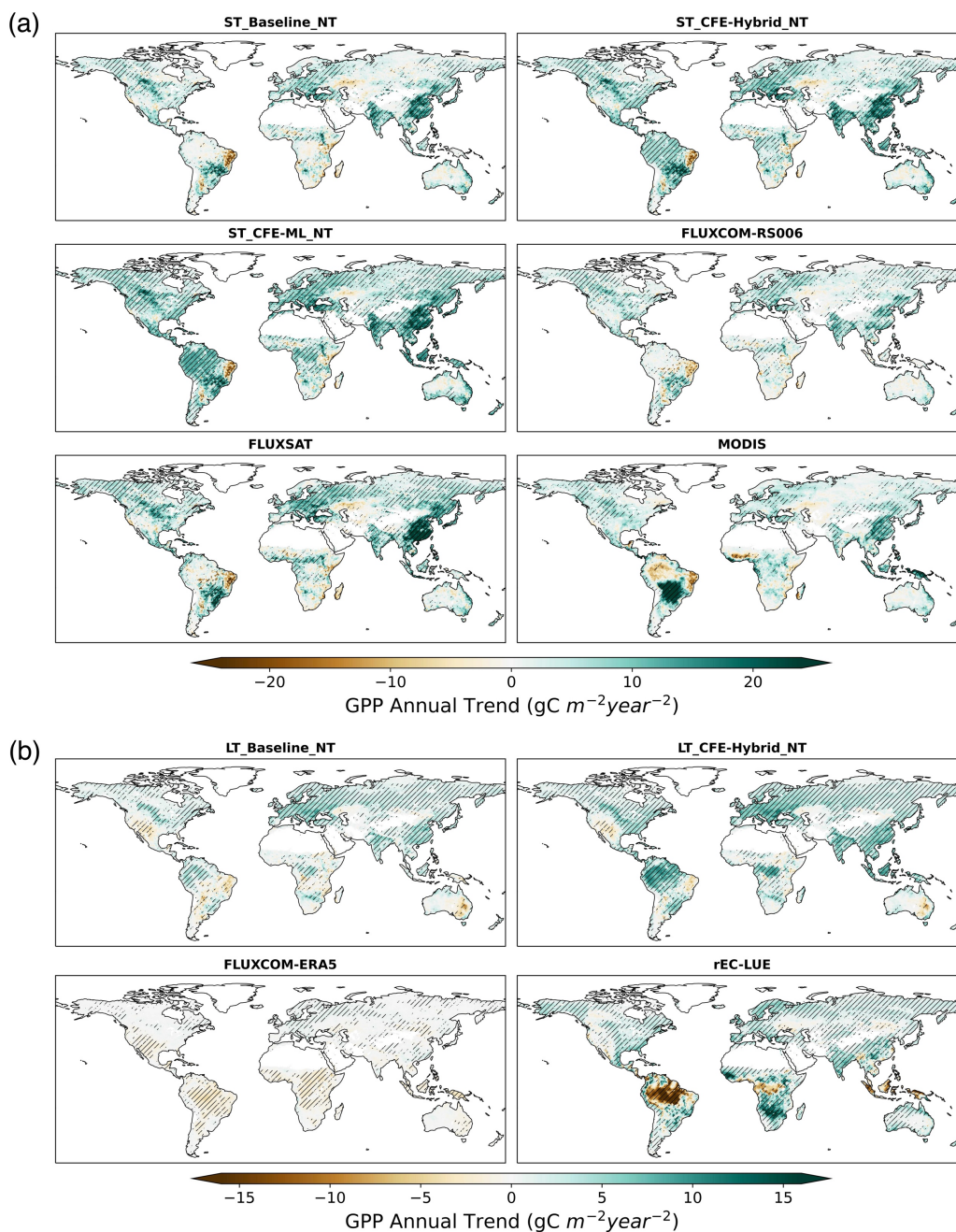
514 Differences in annual GPP trends among CEDAR-GPP model setups and other upscaled and  
 515 LUE-based datasets mainly reflected the variability in the representation of CO<sub>2</sub> fertilization effects  
 516 (Figure 10, Figure S4). From 2001 to 2018, the CEDAR-GPP Baseline model setups showed spatial  
 517 variations in GPP trends consistent with the other upscaled datasets without direct CO<sub>2</sub> fertilization  
 518 effects, including FLUXSAT and FLUXCOM-RSv006. In these datasets, substantial increases were  
 519 seen in southeastern China and India, western Europe, and part of North and South America. These  
 520 increases were largely associated with rising LAI due to land use changes and indirect CO<sub>2</sub>  
 521 fertilization effects, as identified by previous studies (Zhu et al., 2016; Chen et al., 2019). Although  
 522 MODIS, which also does not include a direct CO<sub>2</sub> fertilization effect, generally agreed with these  
 523 increasing trends, it also showed a declining GPP in the tropical Amazon and a stronger positive  
 524 trend in central South America. After incorporating the direct CO<sub>2</sub> fertilization effects, both the  
 525 CFE-Hybrid and CFE-ML setups predicted positive trends in tropical forests, an observation absent  
 526 in all other datasets. Furthermore, the CFE-Hybrid and CFE-ML models also revealed increasing



527 GPP in temperate and boreal forests of North America and Eurasia. Notably, all datasets agreed on  
528 a pronounced GPP decrease in eastern Brazil.

529 From 2001 to 2018, a positive trend in global annual GPP was uniformly detected by all  
530 datasets, albeit with varying magnitudes (Figure 11a-b). The ST\_Baseline\_NT model predicted a  
531 GPP growth rate of 0.35 Pg C per year, aligning with FLUXCOM-RS, but lower than FLUXSAT  
532 (0.51 Pg C yr<sup>-2</sup>) and MODIS (0.39Pg C yr<sup>-2</sup>) (Figure 11b). The CFE-hybrid models estimated a  
533 notably faster GPP growth at 0.58 Pg C yr<sup>-2</sup>. The CFE-ML models predicted the highest trends, up  
534 to 0.76 Pg C yr<sup>-2</sup> from the ST\_CFE-ML\_NT model and 0.59 Pg C yr<sup>-2</sup> from the ST\_CFE-ML\_DT  
535 model. Also, a higher variance was observed among ensemble members in the ST\_CFE-ML setups  
536 compared to the ST\_Baseline and ST\_CFE-Hybrid models.

537 From 1982 to 2018, the LT\_Baseline\_NT model identified increasing GPP trends in large  
538 areas of Europe, East and South Asia, as well as the Northern Amazon (Figure 10b). The pattern  
539 from the LT\_CFE-Hybrid\_NT model aligned closely with the LT\_Baseline\_NT model but  
540 exhibited a stronger positive trend in global tropical areas as well as Eurasian boreal forests. In  
541 contrast, FLUXCOM-ERA5 showed overall negative trends in the tropics, with a small magnitude.  
542 Lastly, rEC-LUE agreed with positive GPP trends identified in CEDAR-GPP in the extratropical  
543 areas, but predicted a pronounced negative trend in the tropics. At the global scale, all the CEDAR-  
544 GPP long-term models predicted a positive global GPP trend (Figure 11d). The LT\_Baseline  
545 models showed a trend of 0.13 to 0.15 Pg C yr<sup>-2</sup>, while the LT\_CFE-Hybrid setups doubled that  
546 rate. rEC-LUE showed a two-phased pattern with a strong increase in GPP from 1982 to 2000 (0.54  
547 Pg C yr<sup>-2</sup>), followed by a decreasing trend after 2001 (-0.20 Pg C yr<sup>-2</sup>) (Figure S5). This resulted in an  
548 overall positive change at a rate comparable to that of the Baseline model. FLUXCOM-ERA5  
549 exhibited a small negative trend.



550

551

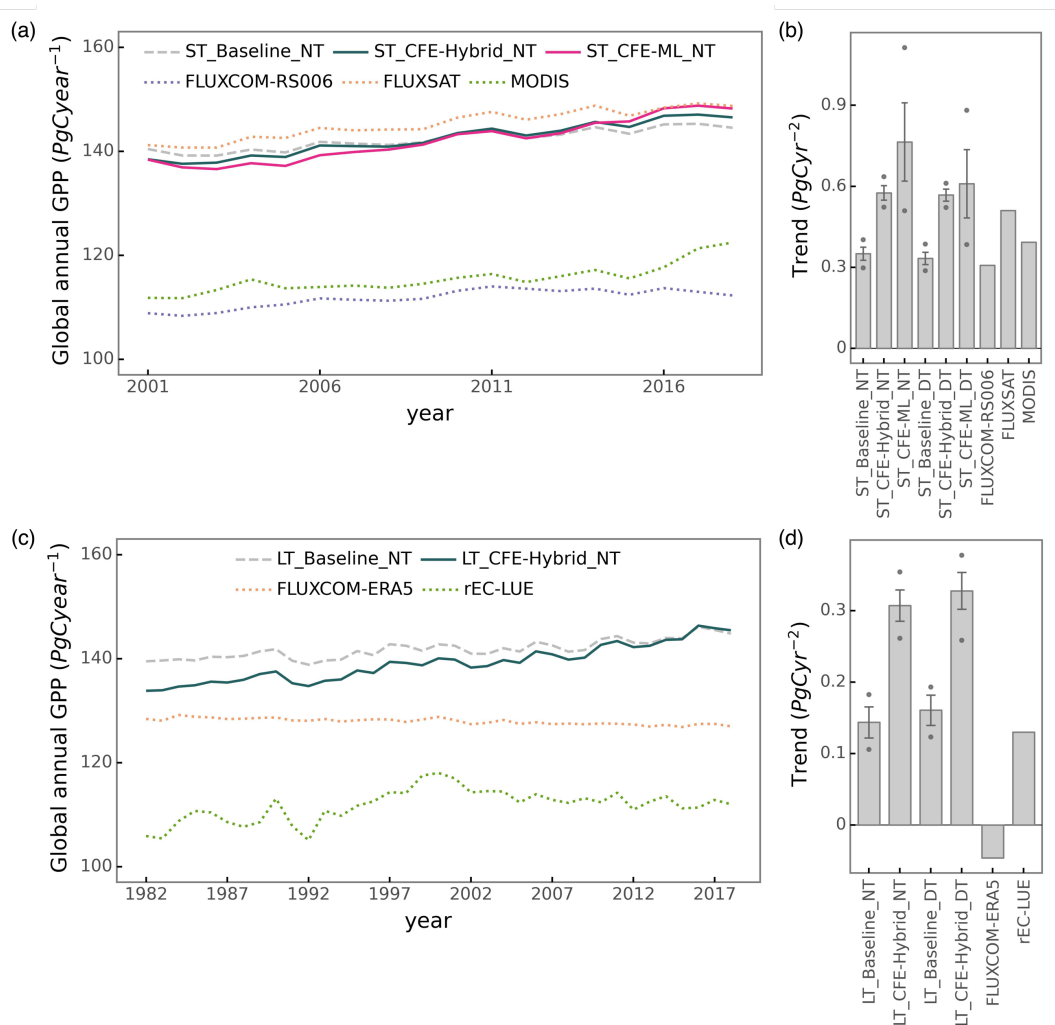
552

553

Figure 10. Annual GPP trend over 2001 – 2018 for short-term CEDAR-GPP, FLUXCOM-RS006, FLUXSAT, and MODIS datasets (a) and over 1982 – 2018 for long-term CEDAR-GPP, FLUXCOM-ERA5 and rEC-LUE datasets (b). Hatched



554 areas indicate the GPP trend that is statistically significant at  $p < 0.05$  level under the  
 555 Mann-Kendal test.



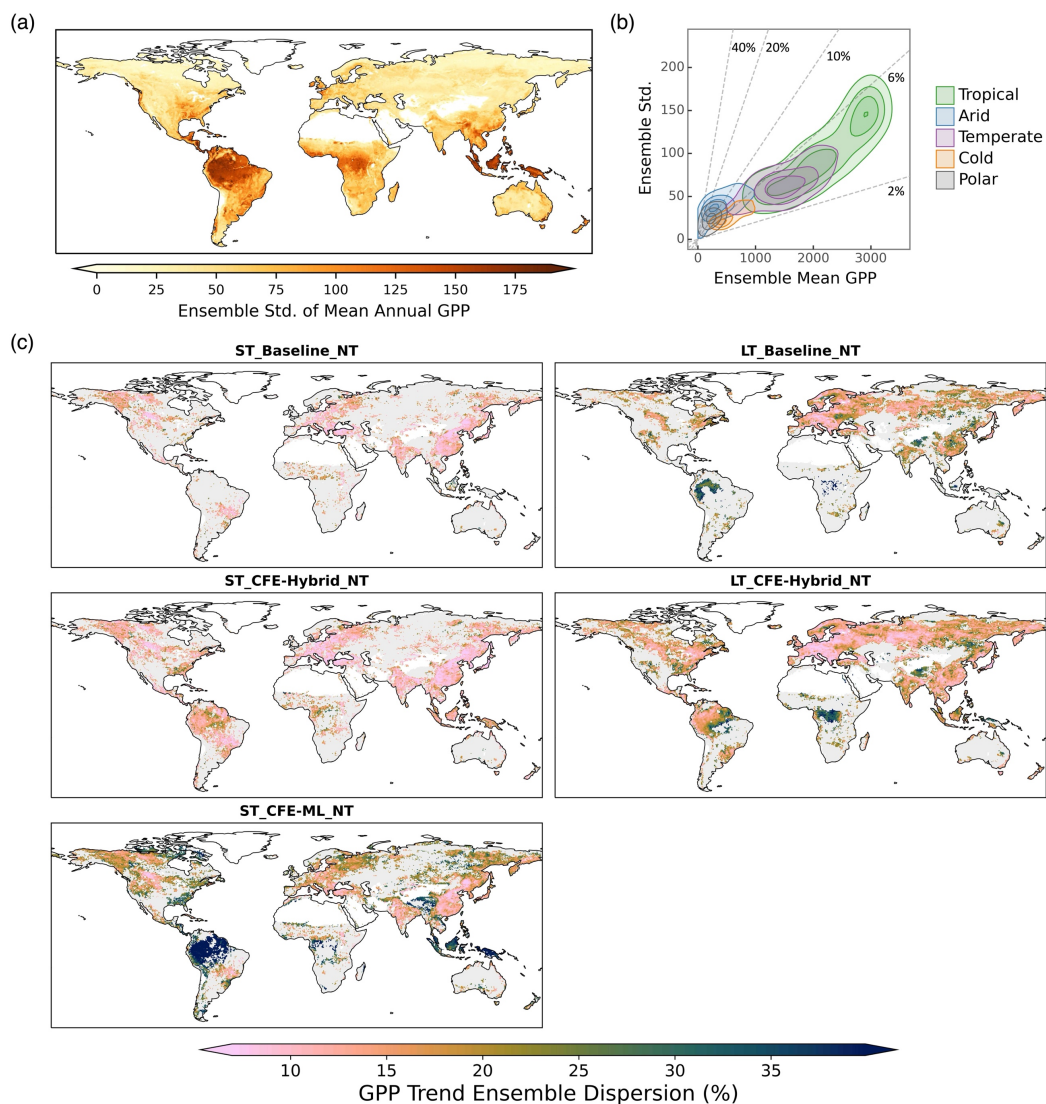
556  
 557 Figure 11. Global annual GPP variations (a) and trends (b) from 2001 to 2018 for  
 558 short-term CEDAR-GPP, FLUXCOM-RS006, FLUXSAT, and MODIS datasets.  
 559 Global annual GPP variations (c) and trends (d) over 1982 to 2018 for long-term  
 560 long-term CEDAR-GPP, FLUXCOM-ERA5, and rEC-LUE datasets. Error bars in  
 561 (b) and (d) represent the 25% to 75% percentile from the model ensembles of  
 562 CEDAR-GPP. Dots in (b) and (d) indicate the minimum and maximum from the  
 563 model ensembles of CEDAR-GPP.

564



### 565 3.3 GPP estimation uncertainties

566 We analyzed the spread between the 30 model ensemble members in CEDAR-GPP as an  
567 indicator of uncertainties in GPP estimations. The spatial pattern of uncertainty in estimating annual  
568 mean GPP largely resembled that of the mean map (Figure 12, Figure 6a). The largest model spread  
569 was found in highly productive tropical forests, and this uncertainty decreased in temperate and cold  
570 areas (Figure 12a). Tropical ecosystems, with a mean annual GPP between 1000 to 3500 PgCyr<sup>-1</sup>,  
571 only exhibited a 2% and 6% variation within the model ensemble (Figure 12b). Ecosystems in the  
572 temperate and cold climates had a smaller annual GPP and proportionally small uncertainties of up  
573 to 6%. However, ecosystems in Arid and Polar climates, despite their similarly low GPP, showed  
574 higher model uncertainty, reaching 10% to 40% of the ensemble mean. The estimation uncertainty  
575 of GPP trends was generally below 15% to 20% in the CEDAR-GPP datasets under the  
576 ST\_Baseline and ST\_CFE-Hybrid setups (Figure 12c). However, in the ST\_CFE-ML setup, the  
577 estimation increased substantially, with model spread reaching up to 40% in tropical areas. Notably,  
578 the long-term models showed a higher uncertainty compared to the short-term models.



579

580

581

582

583

584

585

586

587

588

589

Figure 12. CEDAR-GPP estimation uncertainty derived from ensemble spread (standard deviation of 30 model predictions). (a) Spatial patterns of the absolute standard deviation from ensemble members in estimating the mean annual GPP from 2001 to 2018, using data from the ST\_CFE-Hybrid\_NT setup. (b) Relationships between ensemble standard deviation and ensemble mean in mean annual GPP. Colored contours denote clusters of Koppen climate zones. Dashed lines indicate the ratio between the ensemble standard deviation and the ensemble mean with values shown in percentage. (c) Spatial patterns of model uncertainty in GPP long-term trend estimation. Only areas where 90% of the ensemble members showed a statistically significant trend ( $p < 0.05$ ) are shown in the maps. The trend for the short-term datasets



590 (left column) was computed between 2001 to 2018. The trend for the long-term  
591 datasets (right column) was computed between 1982 to 2018.

## 592 **4. Discussion**

### 593 **4.1 Reducing uncertainties in GPP upscaling**

594 Here we examine the three predominate sources of uncertainties in machine learning  
595 upscaling of GPP: eddy covariance measurements, input datasets, and the machine learning model.  
596 We discuss strategies used in CEDAR-GPP to reduce the impacts of these uncertainties and  
597 highlight potential future research directions.

#### 598 **4.1.1 Eddy covariance data**

599 Uncertainties associated with eddy covariance measurement and data processing can  
600 propagate through the upscaling process. CEDAR-GPP was produced using monthly aggregated  
601 eddy covariance data, where the impact of random errors in half-hourly measurements was  
602 minimized due to the temporal aggregation (Jung et al., 2020). Our stringent quality screening  
603 further reduced data processing uncertainties such as those associated with gap-filling. Yet, the  
604 discrepancy in GPP patterns between the CEDAR-GPP NT and DT setups is indicative of  
605 systematic biases linked to the partitioning approaches used to derive GPP from the Net Ecosystem  
606 Exchange (NEE) measurements (Keenan et al., 2019; Pastorello et al., 2020). Interestingly, the mean  
607 annual GPP from the DT setup was slightly higher than that from the NT setup (Figure 6), and the  
608 DT setup also predicted a higher GPP trend in the long-term dataset (Figure 11). While these  
609 discrepancies were relatively small compared to the predominant spatiotemporal patterns, the  
610 separate DT and NT setups in CEDAR-GPP offered an interesting quantification of the GPP  
611 partitioning uncertainties over space and time, providing insights for future methodology  
612 improvements.

613 The unbalanced spatial representativeness of the eddy covariance data constitutes a more  
614 significant source of uncertainty, as highlighted by previous studies (Tramontana et al., 2015; Jung et  
615 al., 2020). Effective generalization of machine learning models requires a substantial volume of  
616 training data that adequately represents and balances unseen conditions. In CEDAR-GPP, this issue  
617 was mitigated with a large set of eddy covariance data (~18000 site-months) integrating  
618 FLUXNET2015 and two regional networks. However, data availability remains limited in critical



619 carbon exchange hotspots such as tropical, subtropical, and boreal regions, as well as in  
620 mountainous areas (Figure 1). Contrary to widespread perception that sparse training data leads to  
621 high upscaling uncertainties, our findings from the bootstrapped model spread indicated that modest  
622 uncertainties in tropical areas relative to their high GPP magnitude (Figure 12). This observation  
623 aligns with findings from the FLUXCOM product, revealing low extrapolation uncertainty in humid  
624 tropical regions (Jung et al., 2020). Additionally, an early study found that a machine learning model,  
625 when trained with simulated data from a terrestrial biosphere model that matches the locations and  
626 times of FLUXNET sites, could explain 92% of the global variation of GPP (Jung et al., 2009).  
627 These findings suggest that to fully understand the upscaling uncertainty, it is essential to evaluate  
628 the generalization or extrapolation errors within the predictor space, which indicates the  
629 environmental controls and physiological mechanisms of the ecosystem carbon fluxes (van der  
630 Horst et al., 2019; Villarreal and Vargas, 2021). Nevertheless, data limitations in mountainous areas  
631 and the absence of topology information in the predictor space in our models suggest potential  
632 uncertainties related to topographical effects on GPP (Hao et al., 2022; Xie et al., 2023).

633 Furthermore, our analysis suggested that the estimated global GPP magnitudes were related  
634 to the specific eddy covariance GPP data used in upscaling. Notably, global GPP magnitudes  
635 derived from CEDAR-GPP closely aligned with those from FLUXSAT, while the estimates from  
636 FLUXCOM were considerably lower (Figure 6, Figure 11). FLUXSAT used eddy covariance data  
637 from FLUXNET2015, which largely overlapped with that included in CEDAR-GPP (Joiner and  
638 Yoshida, 2020). FLUXCOM utilized data from FLUXNET La Thuile set and CarboAfrica network,  
639 which consisted of a distinct set of sites (Tramontana et al., 2016). The influence from the predictor  
640 datasets was minimal since all three datasets relied on MODIS-derived products. For a more in-  
641 depth evaluation of the impacts of flux site representativeness on upscaling, future research  
642 directions could include conducting synthetic experiments with simulations of ensembles of  
643 terrestrial biosphere models.

#### 644 4.1.2 Input predictors and controlling factors

645 Upscaled GPP inherent uncertainties from the input predictors, including satellite and climate  
646 datasets. First, satellite remote sensing data contains noises resulting from sun-earth geometry,  
647 atmospheric conditions, soil background, and geolocation inaccuracies. The models or algorithms  
648 used for variable estimation, such as those for retrieving LAI, fAPAR, LST, and soil moisture, also  
649 contain random errors and systematic biases specific to certain regions, biome types, or climatic





650 conditions (Yan et al., 2016b; Fang et al., 2019; Ma et al., 2019). Moreover, satellite observations  
651 frequently contain missing values due to clouds, aerosols, snow, and algorithm failure, leading to  
652 both systematic and random uncertainties. In producing CEDAR-GPP, we mitigated these  
653 uncertainties through comprehensive preprocessing procedures. Our temporal gap-filling strategy  
654 exploited both the temporal dependency of vegetation status and long-term climatology, to reduce  
655 biases from missing values. Temporal and spatial aggregation further reduced the remaining data  
656 gaps and random noises. Nevertheless, considerable uncertainties likely remained in satellite datasets  
657 impacting the upscaled estimations.

658 A potentially more impactful source of uncertainty is the mismatch between the footprint of  
659 the eddy covariance measurements and the coarse resolution of satellite observations. While flux  
660 towers typically have a footprint of around  $\sim 1 \text{ km}^2$  (Chu et al., 2021), satellite observations  
661 employed in CEDAR-GPP and most other upscaled datasets were at 5 km or lower resolution.  
662 Systematic and random errors could be introduced due to this mismatch, particularly in  
663 heterogenous biomes and areas with a mixture of vegetation and non-vegetated land covers. One  
664 mitigation strategy is to generate upscaled datasets at a higher spatial resolution (e.g. 500m).  
665 Alternatively, models could be trained at a high resolution and applied to the coarse resolution to  
666 reduce computation and storage requirements (Dannenberg et al., 2023). However, this approach  
667 does not address inherent scaling errors in coarse-resolution satellite images (Yan et al., 2016a; Dong  
668 et al., 2023).

669 Besides the quality of predictors, successful machine learning upscaling also requires a  
670 comprehensive set of features representing all controlling factors. CEDAR-GPP used satellite  
671 observations from optical, thermal, and microwave systems as well as climate variables thoroughly  
672 representing GPP dynamics. Particularly, the inclusion of LST and soil moisture data provides  
673 important information about resource limitations and stress factors, which are crucial for certain  
674 biomes and/or under specific conditions (Stocker et al., 2018, 2019; Green et al., 2022). Dannenberg  
675 et al. (2023) showed that incorporating LST from MODIS and soil moisture from the SMAP  
676 satellite datasets substantially improved the machine learning estimation accuracy of GPP in North  
677 American drylands. Nevertheless, accurately capturing interannual anomalies remain challenging for  
678 certain biomes, such as evergreen needleleaf forest, cropland, and wetland (Figure 4), suggesting that  
679 vital information on GPP is missing or inadequately represented in existing datasets. To this end,  
680 potential improvement may be achieved by incorporating datasets related to agricultural  
681 management practices (crop type, cultivar, irrigation, fertilization) (Xie et al., 2021), plant hydraulic



682 and physiological properties (Liu et al., 2021), root and soil characteristics (Stocker et al., 2023), as  
683 well as topography (Xie et al., 2023).

#### 684 4.1.3 Machine learning models and uncertainty quantification

685 The choice of machine learning models and their parameterization has been found to have a  
686 relatively minor impact on GPP upscaling uncertainties (Tramontana et al., 2015). CEDAR used the  
687 state-of-the-art boosting algorithm, XGBoost, which provided high performance given the current  
688 data availability. Further reduction of model uncertainty will likely rely on additional information,  
689 such as increasing the number of eddy covariance sites or incorporating more high-quality  
690 predictors. Additionally, temporal dependency of carbon fluxes responses to atmospheric controls  
691 may also be exploited with specialized deep neural networks such as recurrent neural networks or  
692 transformers (Besnard et al., 2019; Ma and Liang, 2022).

693 A key challenge, however, is the quantification of uncertainties in machine learning upscaling  
694 (Reichstein et al., 2019). The limited availability of eddy covariance data hinders a comprehensive  
695 assessment of the extrapolation errors; consequently, metrics of predictive performance from cross-  
696 validation are inherently biased. CEDAR derived estimation uncertainty for each GPP prediction  
697 using bootstrapping model ensemble, which naturally mimics the biased sampling of flux tower  
698 locations. Notably, the choice of input climate reanalysis datasets could also induce systematic  
699 differences in GPP spatial and temporal patterns (Tramontana et al., 2015). As a result, the  
700 FLUXCOM product generatec model ensembles based on different reanalysis datasets to capture  
701 these uncertainties. Additionally, different satellite datasets of vegetation structural proxies, such as  
702 LAI, also exhibited significant discrepancies (Jiang et al., 2017). Thus, an ensemble approach  
703 combining site-level bootstrapping with multiple sources of input predictors could potentially  
704 provide a more comprehensive quantification of uncertainties. Future work may also explore  
705 Bayesian neural networks, which provide uncertainty along with predictions and, at the same time,  
706 present high predictive power comparable to ensemble tree-based algorithms (Ma et al., 2021).

#### 707 4.2 Long-term GPP changes and CO<sub>2</sub> fertilization effect

708 CEDAR-GPP was constructed using a comprehensive set of climate variables and multi-  
709 source satellite observations, thus, encapsulating long-term GPP dynamics from both direct and  
710 indirect effects of climate controls. Particularly, CEDAR-GPP included the direct CO<sub>2</sub> fertilization  
711 effect, which has been shown to dominate the increasing trend of global photosynthesis (Chen et al.,



712 2022). Incorporating these effects substantially improved long-term trends of GPP from site to  
713 global scales (Figure 5, 10, 11). CEDAR's CFE-Hybrid setup offered a conservative estimation of  
714 the direct CO<sub>2</sub> effects by simulating the light-limited sensitivity on LUE for C3 plants (Walker et al.,  
715 2021). Nevertheless, the model did not account for the impacts of nutrient availability, which could  
716 potentially constrain CO<sub>2</sub> fertilization (Reich et al., 2014; Peñuelas et al., 2017; Terrer et al., 2019).  
717 Furthermore, the sensitivity of light-limited photosynthesis is a function of temperature, resulting in  
718 the most pronounced increasing trend in the tropics (Figure 10). Yet the model assumed a fixed  
719 ratio of leaf-internal to ambient CO<sub>2</sub>, and thus did not include any responses to vapor pressure  
720 deficit.

721 The CFE-ML model adopted a data-driven approach to infer CO<sub>2</sub> effects directly from eddy  
722 covariance data. This strategy allowed the model to capture any physiological pathways of the CO<sub>2</sub>  
723 impact evidenced in the eddy covariance measurements, including the increases of the biochemical  
724 rates as well as enhancements in the water use efficiency (Keenan et al., 2013). The model  
725 successfully detected a strong positive effect of CO<sub>2</sub> on eddy covariance measured GPP, consistent  
726 with previous studies based on process-based and statistical models (Fernández-Martínez et al.,  
727 2017; Ueyama et al., 2020; Chen et al., 2022). Notably, the CFE-ML model could have included the  
728 impacts of other factors that exhibit a strong temporal correlation with CO<sub>2</sub>. For example,  
729 industrialization-induced increases in nitrogen deposition could synergistically boost GPP alongside  
730 CO<sub>2</sub> (O'Sullivan et al., 2019). Technological and management improvements in agriculture that  
731 contribute to a global boost of crop photosynthesis (Zeng et al., 2014), might also be indirectly  
732 reflected in the model estimates. As a result, the CFE-ML predicted a GPP trend that more closely  
733 aligned with eddy covariance observations, and the upscaled dataset also showed a globally higher  
734 trend than CFE-Hybrid (Figure 5; Figure 10). Nevertheless, spatial patterns of GPP trends from the  
735 CFE-ML aligned with that from CFE-Hybrid, reflecting a strong temperature dependency, implying  
736 that the effects of CO<sub>2</sub> likely remained the most significant factor. Additionally, the considerable  
737 ensemble spread in the CO<sub>2</sub> trends from the CFE-ML model (Figure 11, Figure 13) underscored a  
738 high level of uncertainty in the machine learning quantified CO<sub>2</sub> effects. Future work may exploit  
739 explainable machine learning and causal inference to investigate the underlying mechanisms of CO<sub>2</sub>  
740 effects.



## 741 **5. Data availability**

742 The CEDAR-GPP product, comprising ten GPP datasets, can be accessed at  
743 <https://doi.org/10.5281/zenodo.8212707> (Kang et al., 2023). These datasets were generated at a  
744 spatial resolution of 0.05° and monthly time steps. Each dataset includes an ensemble mean GPP  
745 (“GPP\_mean”) and an ensemble standard deviation (“GPP\_std”). Data is formatted in netCDF  
746 with the following naming convention: “CEDAR-GPP\_<version>\_<model  
747 setup>\_<YYYYMM>.nc”.

## 748 **6. Code availability**

749 The code for upscaling and generating global GPP datasets can be accessed at  
750 <https://doi.org/10.5281/zenodo.8400968>.

## 751 **7. Conclusions**

752 We present the CEDAR-GPP product generated by upscaling global eddy covariance  
753 measurements with machine learning and a broad range of satellite and climate variables. CEDAR-  
754 GPP comprises four long-term datasets from 1982 to 2020 and six short-term datasets from 2001 to  
755 2020. These datasets encompass three configurations regarding the incorporation of direct CO<sub>2</sub>  
756 fertilization effects and two partitioning approaches to derive GPP from eddy covariance data. The  
757 machine learning models of CEDAR-GPP demonstrated high capability in predicting monthly GPP,  
758 its seasonal cycles, and spatial variability within the global eddy covariance sites, with cross-validated  
759 R<sup>2</sup> between 0.56 to 0.79. Short-term model setups consistently outperformed long-term models due  
760 to considerably more and higher-quality information from multi-source satellite observations.

761 CEDAR-GPP advances satellite-based GPP estimations, as the first upscaled dataset that  
762 considered the direct biochemical effects of elevated atmospheric CO<sub>2</sub> on photosynthesis, which is  
763 responsible for an increasing land carbon sink over the past decades. We showed that incorporating  
764 this effect in our CFE-ML and CFE-Hybrid models substantially improved the estimation of GPP  
765 trends at eddy covariance sites. Global patterns of long-term GPP trends in the CFE-ML setups  
766 showed a strong temperature dependency consistent with biophysical theories. Aside from the trend,



767 global spatial and temporal GPP patterns from CEDAR generally aligned with other satellite-based  
768 GPP datasets.

769 In conclusion, CEDAR-GPP, informed by global eddy covariance measurements and a broad  
770 range of multi-source remote sensing observations and climatic variables, offered a comprehensive  
771 representation of global GPP spatial and temporal dynamics over the past four decades. The  
772 different CO<sub>2</sub> fertilization configurations integrated in CEDAR-GPP offer new opportunities for  
773 understanding global ecosystem photosynthesis's response to increases in atmospheric CO<sub>2</sub> along  
774 different pathways over space and time. CEDAR-GPP is expected to serve as a valuable tool for  
775 benchmarking process-based modeling and constraining the global carbon cycle.

776



777 **Appendix A: Photosynthesis sensitivity function of CO<sub>2</sub>**

778 The Light Use Efficiency (LUE) model (Monteith, 1972) of GPP states that,

779 
$$GPP = APAR \times LUE = PAR \times fAPAR \times LUE \quad (A1)$$

780 where  $PAR$  is the photosynthetic active radiation,  $fAPAR$  is the fraction of  $PAR$  that plant canopy  
 781 has absorbed, and  $APAR$  is the absorbed  $PAR$ . Eco-evolutionary theory predicts that the electron-  
 782 transport-limited (light-limited) ( $A_j$ ) and Rubisco-limited ( $A_c$ ) rates of photosynthesis converge on  
 783 the time scale of physiological acclimation, which is in the order of a few weeks. Thus,

784 
$$A = A_c = A_j \quad (A2)$$

785 where  $A$  is the gross photosynthetic rate, here equivalent to GPP.

786 According to the Farquhar, von Caemmerer and Berry (FvCB) model (Farquhar et al., 1980),

787 
$$A_j = \varphi_0 I \frac{c_i - \Gamma^*}{c_i + 2\Gamma^*} \quad (A3)$$

788 where  $\varphi_0$  is the intrinsic quantum efficiency of photosynthesis,  $I$  is the absorbed PAR ( $I = APAR$ ),  
 789  $c_i$  is the leaf-internal partial pressure of CO<sub>2</sub>, and  $\Gamma^*$  is the photorespiratory compensation point that  
 790 depends on temperature:

791 
$$\Gamma^* = r_{25} e^{\frac{\Delta H(T-298.15)}{298.15RT}} \quad (A4)$$

792 where  $r_{25} = 4.22 Pa$  is the photorespiratory point at 25 °C,  $\Delta H$  is the activation energy ( $37.83 \cdot 10^3$   
 793 J mol<sup>-1</sup>),  $T$  is the air temperature in Kelvin, and  $R$  is the molar gas constant ( $8.314 J mol^{-1} K^{-1}$ ). We  
 794 denote atmospheric CO<sub>2</sub> concentration as  $c_a$ , and  $\chi$  is the ratio of leaf internal and external CO<sub>2</sub>, so

795 
$$c_i = \chi c_a \quad (A5)$$

796 Combining (A1), (A3), (A5), and assuming (A2), LUE can be written as,

797 
$$LUE = \varphi_0 \frac{c_i - \Gamma^*}{c_i + 2\Gamma^*} = \varphi_0 \frac{\chi c_a - \Gamma^*}{\chi c_a + 2\Gamma^*} \quad (A6)$$

798 We can therefore show that under constant absorbed light ( $I$  or  $APAR$ ), the sensitivity of GPP to  
 799 CO<sub>2</sub> is proportional to that of LUE,

800 
$$\frac{\partial GPP}{\partial c_a} = \frac{\partial \varphi_0 I \frac{\chi c_a - \Gamma^*}{\chi c_a + 2\Gamma^*}}{\partial c_a} = I \frac{\partial LUE}{\partial c_a} \quad (A7)$$

801 Thus from (A7), we can express the actual GPP at the time  $t$  and a CO<sub>2</sub> level  $c_a^t$  as the product of a  
 802 reference GPP with a CO<sub>2</sub> level  $c_a^0$  and the ratio between actual and reference LUE (A8-9). We

803 denote the actual GPP as time  $t$  as  $GPP_{c_a=c_a^t}^t$ , and the reference GPP at time  $t$  as  $GPP_{c_a=c_a^0}^t$ .



$$804 \quad \frac{GPP_{c_a=c_a^t}^t}{GPP_{c_a=c_a^0}^t} = \frac{LUE_{c_a=c_a^t}^t}{LUE_{c_a=c_a^0}^t} = \frac{\frac{\chi c_a^t - \Gamma^*}{\chi c_a^t + 2\Gamma^*}}{\frac{\chi c_a^0 - \Gamma^*}{\chi c_a^0 + 2\Gamma^*}} = \frac{\phi_{CO_2}^t}{\phi_{CO_2}^{t_0}} \quad (A8)$$

$$805 \quad GPP_{c_a=c_a^t}^t = GPP_{c_a=c_a^0}^t \times \frac{\phi_{CO_2}^t}{\phi_{CO_2}^{t_0}} \quad (A9)$$

806 The reference GPP represents the GPP value at time  $t$  if the  $CO_2$  were at the level of a reference  
807 level, while all other factors, such as  $PAR$ ,  $fAPAR$ , temperature, and other environmental controls  
808 remain unchanged. Here the  $CO_2$  impacts on LUE depend on atmospheric  $CO_2$  ( $c_a$ ),  $\chi$ , and air  
809 temperature. We fixed  $\chi$  to the global average value 0.7 (Prentice et al., 2014; Wang et al., 2017).

810 In the CFE-Hybrid model, we estimated the reference GPP by fixing the  $CO_2$  at the level of the  
811 year 2001 while keeping all other variables dynamic in the CFE-ML model. Then the actual GPP can  
812 be estimated following (A9). Fixing  $CO_2$  values to the 2001 level, the start year of eddy covariance  
813 data used in model training, essentially removed the effects of  $CO_2$  inferred by the CFE-ML model.

## 814 Supplement

815 The supplement related to this article is available online.

## 816 Author contributions

817 T. K. and Y. K. conceptualized the study. Y. K. performed the formal analysis and generated  
818 the final product. Y. K., T. K., M. B., and M. G. contributed to the development and investigation  
819 of the research. Y. K., M. G., and X. L. contributed to data curation and processing. Y. K. prepared  
820 the manuscript with contributions from all co-authors. T. K. supervised the project.

## 821 Acknowledgments

822 We are grateful to Dr. Youngryel Ryu for providing the BESS\_Rad dataset and Dr. Martin  
823 Jung for sharing the FLUXCOM-RS006 dataset. We also thank Dr. Muyi Li for sharing early  
824 versions of the PKU GIMMS NDVI4g and LAI4g datasets with us.

## 825 Financial support

826 This research was supported by the U.S. Department of Energy Office of Science Early  
827 Career Research Program award #DE-SC0021023 and a NASA Award 80NSSC21K1705. TFK  
828 acknowledges additional support from the LEMON'TREE (Land Ecosystem Models based On New  
829 Theory, observations and Experiments) project, funded through the generosity of Eric and Wendy



830 Schmidt by recommendation of the Schmidt Futures programme and NASA award  
831 #80NSSC20K1801.

## 832 **References**

- 833 Anav, A., Friedlingstein, P., Beer, C., Ciais, P., Harper, A., Jones, C., Murray-Tortarolo, G., Papale,  
834 D., Parazoo, N. C., Peylin, P., Piao, S., Sitch, S., Viovy, N., Wiltshire, A., and Zhao, M.:  
835 Spatiotemporal patterns of terrestrial gross primary production: A review, *Reviews of*  
836 *Geophysics*, 1–34, <https://doi.org/10.1002/2015RG000483>, 2015.
- 837 Badgley, G., Anderegg, L. D. L., Berry, J. A., and Field, C. B.: Terrestrial gross primary production:  
838 Using NIRV to scale from site to globe, *Global Change Biology*, 25, 3731–3740,  
839 <https://doi.org/10.1111/gcb.14729>, 2019.
- 840 Baldocchi, D. D.: How eddy covariance flux measurements have contributed to our understanding  
841 of Global Change Biology, *Global Change Biology*, 26, 242–260,  
842 <https://doi.org/10.1111/gcb.14807>, 2020.
- 843 Beck, H. E., Zimmermann, N. E., McVicar, T. R., Vergopolan, N., Berg, A., and Wood, E. F.:  
844 Present and future köppen-geiger climate classification maps at 1-km resolution, *Scientific Data*,  
845 5, 1–12, <https://doi.org/10.1038/sdata.2018.214>, 2018.
- 846 Beer, C., Reichstein, M., Tomelleri, E., Ciais, P., Jung, M., Carvalhais, N., Rödenbeck, C., Arain, M.  
847 A., Baldocchi, D., Bonan, G. B., Bondeau, A., Cescatti, A., Lasslop, G., Lindroth, A., Lomas, M.,  
848 Luyssaert, S., Margolis, H., Oleson, K. W., Rouspard, O., Veenendaal, E., Viovy, N., Williams, C.,  
849 Woodward, F. I., and Papale, D.: Terrestrial gross carbon dioxide uptake: Global distribution and  
850 covariation with climate, *Science*, 329, 834–838, <https://doi.org/10.1126/science.1184984>, 2010.
- 851 Berdugo, M., Gaitán, J. J., Delgado-Baquerizo, M., Crowther, T. W., and Dakos, V.: Prevalence and  
852 drivers of abrupt vegetation shifts in global drylands, *Proceedings of the National Academy of*  
853 *Sciences*, 119, e2123393119, <https://doi.org/10.1073/pnas.2123393119>, 2022.
- 854 Besnard, S., Carvalhais, N., Altaf Arain, M., Black, A., Brede, B., Buchmann, N., Chen, J., Clevers, J.  
855 G. P. W., Dutrieux, L. P., Gans, F., Herold, M., Jung, M., Kosugi, Y., Knohl, A., Law, B. E.,  
856 Paul-Limoges, E., Lohila, A., Merbold, L., Rouspard, O., Valentini, R., Wolf, S., Zhang, X., and  
857 Reichstein, M.: Memory effects of climate and vegetation affecting net ecosystem CO<sub>2</sub> fluxes in  
858 global forests, *PLoS ONE*, 14, 1–22, <https://doi.org/10.1371/journal.pone.0211510>, 2019.
- 859 Bloomfield, K. J., Stocker, B. D., Keenan, T. F., and Prentice, I. C.: Environmental controls on the  
860 light use efficiency of terrestrial gross primary production, *Global Change Biology*, 29, 1037–  
861 1053, <https://doi.org/10.1111/gcb.16511>, 2023.
- 862 Campbell, J. E., Berry, J. A., Seibt, U., Smith, S. J., Montzka, S. A., Launois, T., Belviso, S., Bopp, L.,  
863 and Laine, M.: Large historical growth in global terrestrial gross primary production, *Nature*, 544,  
864 84–87, <https://doi.org/10.1038/nature22030>, 2017.
- 865 Camps-Valls, G., Campos-Taberner, M., Moreno-Martínez, Á., Walther, S., Duveiller, G., Cescatti,  
866 A., Mahecha, M. D., Muñoz-Marí, J., García-Haro, F. J., Guanter, L., Jung, M., Gamon, J. A.,





- 867 Reichstein, M., and Running, S. W.: A unified vegetation index for quantifying the terrestrial  
868 biosphere, *Science Advances*, 7, eabc7447, <https://doi.org/10.1126/sciadv.abc7447>, 2021.
- 869 Cao, S., Li, M., Zhu, Z., Zha, J., Zhao, W., Duanmu, Z., Chen, J., Zheng, Y., and Chen, Y.:  
870 Spatiotemporally consistent global dataset of the GIMMS Leaf Area Index (GIMMS LAI4g)  
871 from 1982 to 2020, *Earth System Science Data Discussions*, 1–31, [https://doi.org/10.5194/essd-](https://doi.org/10.5194/essd-2023-68)  
872 2023-68, 2023.
- 873 Chen, C., Park, T., Wang, X., Piao, S., Xu, B., Chaturvedi, R. K., Fuchs, R., Brovkin, V., Ciais, P.,  
874 Fensholt, R., Tømmervik, H., Bala, G., Zhu, Z., Nemani, R. R., and Myneni, R. B.: China and  
875 India lead in greening of the world through land-use management, *Nature Sustainability*, 2, 122–  
876 129, <https://doi.org/10.1038/s41893-019-0220-7>, 2019.
- 877 Chen, C., Riley, W. J., Prentice, I. C., and Keenan, T. F.: CO<sub>2</sub> fertilization of terrestrial  
878 photosynthesis inferred from site to global scales, *Proceedings of the National Academy of*  
879 *Sciences*, 119, 1–8, <https://doi.org/10.1073/pnas.2115627119/>, 2022.
- 880 Chen, T. and Guestrin, C.: XGBoost: a scalable tree boosting system, in: *Proceedings of the 22nd*  
881 *ACM SIGKDD International Conference on Knowledge Discovery and Data Mining -*  
882 *KDD '16*, 785–794, <https://doi.org/10.1145/2939672.2939785>, 2016.
- 883 Chu, H., Luo, X., Ouyang, Z., Chan, W. S., Dengel, S., Biraud, S. C., Torn, M. S., Metzger, S.,  
884 Kumar, J., Arain, M. A., Arkebauer, T. J., Baldocchi, D., Bernacchi, C., Billesbach, D., Black, T.  
885 A., Blanken, P. D., Bohrer, G., Bracho, R., Brown, S., Brunsell, N. A., Chen, J., Chen, X., Clark,  
886 K., Desai, A. R., Duman, T., Durden, D., Fares, S., Forbrich, I., Gamon, J. A., Gough, C. M.,  
887 Griffis, T., Helbig, M., Hollinger, D., Humphreys, E., Ikawa, H., Iwata, H., Ju, Y., Knowles, J. F.,  
888 Knox, S. H., Kobayashi, H., Kolb, T., Law, B., Lee, X., Litvak, M., Liu, H., Munger, J. W.,  
889 Noormets, A., Novick, K., Oberbauer, S. F., Oechel, W., Oikawa, P., Papuga, S. A., Pendall, E.,  
890 Prajapati, P., Prueger, J., Quinton, W. L., Richardson, A. D., Russell, E. S., Scott, R. L., Starr, G.,  
891 Staebler, R., Stoy, P. C., Stuart-Haëntjens, E., Sonnentag, O., Sullivan, R. C., Suyker, A., Ueyama,  
892 M., Vargas, R., Wood, J. D., and Zona, D.: Representativeness of Eddy-Covariance flux  
893 footprints for areas surrounding AmeriFlux sites, *Agricultural and Forest Meteorology*, 301–302,  
894 <https://doi.org/10.1016/j.agrformet.2021.108350>, 2021.
- 895 Dannenberg, M. P., Barnes, M. L., Smith, W. K., Johnston, M. R., Meerdink, S. K., Wang, X., Scott,  
896 R. L., and Biederman, J. A.: Upscaling dryland carbon and water fluxes with artificial neural  
897 networks of optical, thermal, and microwave satellite remote sensing, *Biogeosciences*, 20, 383–  
898 404, <https://doi.org/10.5194/bg-20-383-2023>, 2023.
- 899 De Kauwe, M. G., Medlyn, B. E., Zaehle, S., Walker, A. P., Dietze, M. C., Hickler, T., Jain, A. K.,  
900 Luo, Y., Parton, W. J., Prentice, I. C., Smith, B., Thornton, P. E., Wang, S., Wang, Y.-P., Wårlind,  
901 D., Weng, E., Crous, K. Y., Ellsworth, D. S., Hanson, P. J., Seok Kim, H., Warren, J. M., Oren,  
902 R., and Norby, R. J.: Forest water use and water use efficiency at elevated CO<sub>2</sub>: a model-data  
903 intercomparison at two contrasting temperate forest FACE sites, *Global Change Biology*, 19,  
904 1759–1779, <https://doi.org/10.1111/gcb.12164>, 2013.



- 905 De Kauwe, M. G., Keenan, T. F., Medlyn, B. E., Prentice, I. C., and Terrer, C.: Satellite based  
906 estimates underestimate the effect of CO<sub>2</sub> fertilization on net primary productivity, *Nature*  
907 *Climate Change*, 6, 892–893, <https://doi.org/10.1038/nclimate3105>, 2016.
- 908 Dong, Y., Li, J., Jiao, Z., Liu, Q., Zhao, J., Xu, B., Zhang, H., Zhang, Z., Liu, C., Knyazikhin, Y., and  
909 Myneni, R. B.: A Method for Retrieving Coarse-Resolution Leaf Area Index for Mixed Biomes  
910 Using a Mixed-Pixel Correction Factor, *IEEE Transactions on Geoscience and Remote Sensing*,  
911 61, 1–17, <https://doi.org/10.1109/TGRS.2023.3235949>, 2023.
- 912 Dorigo, W., Wagner, W., Albergel, C., Albrecht, F., Balsamo, G., Brocca, L., Chung, D., Ertl, M.,  
913 Forkel, M., Gruber, A., Haas, E., Hamer, P. D., Hirschi, M., Ikonen, J., de Jeu, R., Kidd, R.,  
914 Lahoz, W., Liu, Y. Y., Miralles, D., Mistelbauer, T., Nicolai-Shaw, N., Parinussa, R., Pratola, C.,  
915 Reimer, C., van der Schalie, R., Seneviratne, S. I., Smolander, T., and Lecomte, P.: ESA CCI Soil  
916 Moisture for improved Earth system understanding: State-of-the art and future directions,  
917 *Remote Sensing of Environment*, 203, 185–215, <https://doi.org/10.1016/j.rse.2017.07.001>,  
918 2017.
- 919 Dorigo, W. A., Gruber, A., De Jeu, R. A. M., Wagner, W., Stacke, T., Loew, A., Albergel, C., Brocca,  
920 L., Chung, D., Parinussa, R. M., and Kidd, R.: Evaluation of the ESA CCI soil moisture product  
921 using ground-based observations, *Remote Sensing of Environment*, 162,  
922 <https://doi.org/10.1016/j.rse.2014.07.023>, 2015.
- 923 Ehlers, I., Augusti, A., Betson, T. R., Nilsson, M. B., Marshall, J. D., and Schleucher, J.: Detecting  
924 long-term metabolic shifts using isotopomers: CO<sub>2</sub>-driven suppression of photorespiration in C<sub>3</sub>  
925 plants over the 20th century, *Proceedings of the National Academy of Sciences*, 112, 15585–  
926 15590, <https://doi.org/10.1073/pnas.1504493112>, 2015.
- 927 Fang, H., Baret, F., Plummer, S., and Schaepman-Strub, G.: An overview of global leaf area index  
928 (LAI): Methods, products, validation, and applications, *Reviews of Geophysics*, 2018RG000608,  
929 <https://doi.org/10.1029/2018RG000608>, 2019.
- 930 Farquhar, G. D., von Caemmerer, S., and Berry, J. A.: A biochemical model of photosynthetic CO<sub>2</sub>  
931 assimilation in leaves of C<sub>3</sub> species, *Planta*, 149, 78–90, <https://doi.org/10.1007/BF00386231>,  
932 1980.
- 933 Fernández-Martínez, M., Vicca, S., Janssens, I. A., Ciais, P., Obersteiner, M., Bartrons, M., Sardans,  
934 J., Verger, A., Canadell, J. G., Chevallier, F., Wang, X., Bernhofer, C., Curtis, P. S., Gianelle, D.,  
935 Grünwald, T., Heinesch, B., Ibrom, A., Knohl, A., Laurila, T., Law, B. E., Limousin, J. M.,  
936 Longdoz, B., Loustau, D., Mammarella, I., Matteucci, G., Monson, R. K., Montagnani, L., Moors,  
937 E. J., Munger, J. W., Papale, D., Piao, S. L., and Peñuelas, J.: Atmospheric deposition, CO<sub>2</sub>, and  
938 change in the land carbon sink, *Sci Rep*, 7, 9632, <https://doi.org/10.1038/s41598-017-08755-8>,  
939 2017.
- 940 Friedl, M. and Sulla-Menashe, D.: MCD12Q1 MODIS/Terra+Aqua Land Cover Type Yearly L3  
941 Global 500m SIN Grid V006 [Data set], NASA EOSDIS Land Processes DAAC,  
942 <https://doi.org/10.5067/MODIS/MCD12Q1.006>, 2019.



- 943 Friedlingstein, P., Meinshausen, M., Arora, V. K., Jones, C. D., Anav, A., Liddicoat, S. K., and  
944 Knutti, R.: Uncertainties in CMIP5 climate projections due to carbon cycle feedbacks, *Journal of*  
945 *Climate*, 27, 511–526, <https://doi.org/10.1175/JCLI-D-12-00579.1>, 2014.
- 946 Friedlingstein, P., O’Sullivan, M., Jones, M. W., Andrew, R. M., Gregor, L., Hauck, J., Le Quéré, C.,  
947 Luijkx, I. T., Olsen, A., Peters, G. P., Peters, W., Pongratz, J., Schwingshackl, C., Sitch, S.,  
948 Canadell, J. G., Ciais, P., Jackson, R. B., Alin, S. R., Alkama, R., Arneeth, A., Arora, V. K., Bates,  
949 N. R., Becker, M., Bellouin, N., Bittig, H. C., Bopp, L., Chevallier, F., Chini, L. P., Cronin, M.,  
950 Evans, W., Falk, S., Feely, R. A., Gasser, T., Gehlen, M., Gkritzalis, T., Gloege, L., Grassi, G.,  
951 Gruber, N., Gürses, Ö., Harris, I., Hefner, M., Houghton, R. A., Hurtt, G. C., Iida, Y., Ilyina, T.,  
952 Jain, A. K., Jersild, A., Kadono, K., Kato, E., Kennedy, D., Klein Goldewijk, K., Knauer, J.,  
953 Korsbakken, J. I., Landschützer, P., Lefèvre, N., Lindsay, K., Liu, J., Liu, Z., Marland, G., Mayot,  
954 N., McGrath, M. J., Metzl, N., Monacci, N. M., Munro, D. R., Nakaoka, S.-I., Niwa, Y., O’Brien,  
955 K., Ono, T., Palmer, P. I., Pan, N., Pierrot, D., Pockock, K., Poulter, B., Resplandy, L., Robertson,  
956 E., Rödenbeck, C., Rodriguez, C., Rosan, T. M., Schwinger, J., Séférian, R., Shutler, J. D.,  
957 Skjelvan, I., Steinhoff, T., Sun, Q., Sutton, A. J., Sweeney, C., Takao, S., Tanhua, T., Tans, P. P.,  
958 Tian, X., Tian, H., Tilbrook, B., Tsujino, H., Tubiello, F., van der Werf, G. R., Walker, A. P.,  
959 Wanninkhof, R., Whitehead, C., Willstrand Wranne, A., et al.: Global Carbon Budget 2022, *Earth*  
960 *System Science Data*, 14, 4811–4900, 2023.
- 961 Gampe, D., Zscheischler, J., Reichstein, M., Sullivan, M. O., Smith, W. K., Sitch, S., and Buermann,  
962 W.: Increasing impact of warm droughts on northern ecosystem productivity over recent  
963 decades, *Nature Climate Change*, <https://doi.org/10.1038/s41558-021-01112-8>, 2021.
- 964 Gao, B. C.: NDWI - A normalized difference water index for remote sensing of vegetation liquid  
965 water from space, *Remote Sensing of Environment*, 58, 257–266,  
966 [https://doi.org/10.1016/S0034-4257\(96\)00067-3](https://doi.org/10.1016/S0034-4257(96)00067-3), 1996.
- 967 Gitelson, A. A.: Remote estimation of leaf area index and green leaf biomass in maize canopies,  
968 *Geophysical Research Letters*, 30, 1248, <https://doi.org/10.1029/2002GL016450>, 2003.
- 969 Green, J. K., Ballantyne, A., Abramoff, R., Gentine, P., Makowski, D., and Ciais, P.: Surface  
970 temperatures reveal the patterns of vegetation water stress and their environmental drivers across  
971 the tropical Americas, *Global Change Biology*, 28, 2940–2955,  
972 <https://doi.org/10.1111/gcb.16139>, 2022.
- 973 Gruber, A., Scanlon, T., Van Der Schalie, R., Wagner, W., and Dorigo, W.: Evolution of the ESA  
974 CCI Soil Moisture climate data records and their underlying merging methodology, *Earth System*  
975 *Science Data*, 11, 717–739, <https://doi.org/10.5194/essd-11-717-2019>, 2019.
- 976 Hao, D., Bisht, G., Huang, M., Ma, P.-L., Tesfa, T., Lee, W.-L., Gu, Y., and Leung, L. R.: Impacts of  
977 Sub-Grid Topographic Representations on Surface Energy Balance and Boundary Conditions in  
978 the E3SM Land Model: A Case Study in Sierra Nevada, *Journal of Advances in Modeling Earth*  
979 *Systems*, 14, e2021MS002862, <https://doi.org/10.1029/2021MS002862>, 2022.
- 980 Haverd, V., Smith, B., Canadell, J. G., Cuntz, M., Mikaloff-Fletcher, S., Farquhar, G., Woodgate, W.,  
981 Briggs, P. R., and Trudinger, C. M.: Higher than expected CO<sub>2</sub> fertilization inferred from leaf to



- 982 global observations, *Global Change Biology*, 26, 2390–2402, <https://doi.org/10.1111/gcb.14950>,  
983 2020.
- 984 van der Horst, S. V. J., Pitman, A. J., De Kauwe, M. G., Ukkola, A., Abramowitz, G., and Isaac, P.:  
985 How representative are FLUXNET measurements of surface fluxes during temperature  
986 extremes?, *Biogeosciences*, 16, 1829–1844, <https://doi.org/10.5194/bg-16-1829-2019>, 2019.
- 987 Jiang, C., Ryu, Y., Fang, H., Myneni, R., Claverie, M., and Zhu, Z.: Inconsistencies of interannual  
988 variability and trends in long-term satellite leaf area index products, *Global Change Biology*, 23,  
989 4133–4146, <https://doi.org/10.1111/gcb.13787>, 2017.
- 990 Joiner, J. and Yoshida, Y.: Satellite-based reflectances capture large fraction of variability in global  
991 gross primary production (GPP) at weekly time scales, *Agricultural and Forest Meteorology*, 291,  
992 108092, <https://doi.org/10.1016/j.agrformet.2020.108092>, 2020.
- 993 Jung, M., Reichstein, M., and Bondeau, A.: Towards global empirical upscaling of FLUXNET eddy  
994 covariance observations: Validation of a model tree ensemble approach using a biosphere model,  
995 *Biogeosciences*, 6, 2001–2013, <https://doi.org/10.5194/bg-6-2001-2009>, 2009.
- 996 Jung, M., Reichstein, M., Margolis, H. A., Cescatti, A., Richardson, A. D., Arain, M. A., Arneth, A.,  
997 Bernhofer, C., Bonal, D., Chen, J., Gianelle, D., Gobron, N., Kiely, G., Kutsch, W., Lasslop, G.,  
998 Law, B. E., Lindroth, A., Merbold, L., Montagnani, L., Moors, E. J., Papale, D., Sottocornola, M.,  
999 Vaccari, F., and Williams, C.: Global patterns of land-atmosphere fluxes of carbon dioxide , latent  
1000 heat , and sensible heat derived from eddy covariance , satellite , and meteorological observations,  
1001 *Journal of Geophysical Research: Biogeosciences*, 116, 1–16,  
1002 <https://doi.org/10.1029/2010JG001566>, 2011.
- 1003 Jung, M., Reichstein, M., Schwalm, C. R., Huntingford, C., Sitch, S., Ahlström, A., Arneth, A.,  
1004 Camps-Valls, G., Ciais, P., Friedlingstein, P., Gans, F., Ichii, K., Jain, A. K., Kato, E., Papale, D.,  
1005 Poulter, B., Raduly, B., Rödenbeck, C., Tramontana, G., Viovy, N., Wang, Y. P., Weber, U.,  
1006 Zaehle, S., and Zeng, N.: Compensatory water effects link yearly global land CO<sub>2</sub> sink changes  
1007 to temperature, *Nature*, 541, 516–520, <https://doi.org/10.1038/nature20780>, 2017.
- 1008 Jung, M., Schwalm, C., Migliavacca, M., Walther, S., Camps-Valls, G., Koirala, S., Anthoni, P.,  
1009 Besnard, S., Bodesheim, P., Carvalhais, N., Chevallier, F., Gans, F., S Goll, D., Haverd, V.,  
1010 Köhler, P., Ichii, K., K Jain, A., Liu, J., Lombardozzi, D., E M S Nabel, J., A Nelson, J.,  
1011 O’Sullivan, M., Pallandt, M., Papale, D., Peters, W., Pongratz, J., Rödenbeck, C., Sitch, S.,  
1012 Tramontana, G., Walker, A., Weber, U., and Reichstein, M.: Scaling carbon fluxes from eddy  
1013 covariance sites to globe: Synthesis and evaluation of the FLUXCOM approach, *Biogeosciences*,  
1014 17, 1343–1365, <https://doi.org/10.5194/bg-17-1343-2020>, 2020.
- 1015 Kang, Y., Ozdogan, M., Zhu, X., Ye, Z., Hain, C., and Anderson, M.: Comparative assessment of  
1016 environmental variables and machine learning algorithms for maize yield prediction in the US  
1017 Midwest, *Environmental Research Letters*, 15, <https://doi.org/10.1088/1748-9326/ab7df9>,  
1018 2020.



- 1019 Kang, Y., Gaber, M., Bassiouni, M., Lu, X., and Keenan, T.: CEDAR-GPP: A Spatiotemporally  
1020 Upscaled Dataset of Gross Primary Productivity Incorporating CO<sub>2</sub> Fertilization (v1.0),  
1021 <https://doi.org/10.5281/zenodo.8212707>, 2023.
- 1022 Keeling, R. F., Graven, H. D., Welp, L. R., Resplandy, L., Bi, J., Piper, S. C., Sun, Y., Bollenbacher,  
1023 A., and Meijer, H. A. J.: Atmospheric evidence for a global secular increase in carbon isotopic  
1024 discrimination of land photosynthesis, *Proceedings of the National Academy of Sciences of the*  
1025 *United States of America*, 114, 10361–10366, <https://doi.org/10.1073/pnas.1619240114>, 2017.
- 1026 Keenan, T. F. and Williams, C. A.: The terrestrial carbon sink, *Annual Review of Environment and*  
1027 *Resources*, 43, 219–243, <https://doi.org/10.1146/annurev-environ-102017-030204>, 2018.
- 1028 Keenan, T. F., Hollinger, D. Y., Bohrer, G., Dragoni, D., Munger, J. W., Schmid, H. P., and  
1029 Richardson, A. D.: Increase in forest water-use efficiency as atmospheric carbon dioxide  
1030 concentrations rise, *Nature*, 499, 324–327, <https://doi.org/10.1038/nature12291>, 2013.
- 1031 Keenan, T. F., Prentice, I. C., Canadell, J. G., Williams, C. A., Wang, H., Raupach, M., and Collatz,  
1032 G. J.: Recent pause in the growth rate of atmospheric CO<sub>2</sub> due to enhanced terrestrial carbon  
1033 uptake, *Nature Communications*, 7, 1–9, <https://doi.org/10.1038/ncomms13428>, 2016.
- 1034 Keenan, T. F., Migliavacca, M., Papale, D., Baldocchi, D., Reichstein, M., Torn, M., and Wutzler, T.:  
1035 Widespread inhibition of daytime ecosystem respiration, *Nature Ecology and Evolution*, 3, 407–  
1036 415, <https://doi.org/10.1038/s41559-019-0809-2>, 2019.
- 1037 Li, M., Cao, S., and Zhu, Z.: Spatiotemporally consistent global dataset of the GIMMS Normalized  
1038 Difference Vegetation Index (PKU GIMMS NDVI) from 1982 to 2020, *Earth System Science*  
1039 *Data Discussions*, 1–31, <https://doi.org/10.5194/essd-2023-1>, 2023.
- 1040 Liu, Y., Holtzman, N. M., and Konings, A. G.: Global ecosystem-scale plant hydraulic traits  
1041 retrieved using model–data fusion, *Hydrology and Earth System Sciences*, 25, 2399–2417,  
1042 <https://doi.org/10.5194/hess-25-2399-2021>, 2021.
- 1043 Ma, H. and Liang, S.: Development of the GLASS 250-m leaf area index product (version 6) from  
1044 MODIS data using the bidirectional LSTM deep learning model, *Remote Sensing of*  
1045 *Environment*, 273, 112985, <https://doi.org/10.1016/j.rse.2022.112985>, 2022.
- 1046 Ma, H., Zeng, J., Chen, N., Zhang, X., Cosh, M. H., and Wang, W.: Satellite surface soil moisture  
1047 from SMAP, SMOS, AMSR2 and ESA CCI: A comprehensive assessment using global ground-  
1048 based observations, *Remote Sensing of Environment*, 231, 111215,  
1049 <https://doi.org/10.1016/j.rse.2019.111215>, 2019.
- 1050 Ma, Y., Zhang, Z., Kang, Y., and Özdoğan, M.: Corn yield prediction and uncertainty analysis based  
1051 on remotely sensed variables using a Bayesian neural network approach, *Remote Sensing of*  
1052 *Environment*, 259, 112408, <https://doi.org/10.1016/j.rse.2021.112408>, 2021.
- 1053 Myneni, R., Knyazikhin, Y., and Park, T.: MCD15A3H MODIS/Terra+Aqua Leaf Area  
1054 Index/FPAR 4-day L4 Global 500m SIN Grid V006 [Data set], NASA EOSDIS Land Processes  
1055 DAAC., <https://doi.org/10.5067/MODIS/MCD15A3H.006>, 2015a.



- 1056 Myneni, R., Knyazikhin, Y., and Park, T.: MOD15A2H MODIS/Terra Leaf Area Index/FPAR 8-  
1057 Day L4 Global 500m SIN Grid V006 [Data set], NASA EOSDIS Land Processes DAAC,  
1058 [https://doi.org/10.5067/MODIS/MOD15A2H.006\\_2015b](https://doi.org/10.5067/MODIS/MOD15A2H.006_2015b).
- 1059 O'Sullivan, M., Spracklen, D. V., Batterman, S. A., Arnold, S. R., Gloor, M., and Buermann, W.:  
1060 Have Synergies Between Nitrogen Deposition and Atmospheric CO<sub>2</sub> Driven the Recent  
1061 Enhancement of the Terrestrial Carbon Sink?, *Global Biogeochemical Cycles*, 33, 163–180,  
1062 <https://doi.org/10.1029/2018GB005922>, 2019.
- 1063 O'Sullivan, M., Smith, W. K., Sitch, S., Friedlingstein, P., Arora, V. K., Haverd, V., Jain, A. K., Kato,  
1064 E., Kautz, M., Lombardozzi, D., Nabel, J. E. M. S., Tian, H., Vuichard, N., Wiltshire, A., Zhu,  
1065 D., and Buermann, W.: Climate-Driven Variability and Trends in Plant Productivity Over Recent  
1066 Decades Based on Three Global Products, *Global Biogeochemical Cycles*, 34,  
1067 <https://doi.org/10.1029/2020GB006613>, 2020.
- 1068 Pastorello, G., Trotta, C., Canfora, E., Chu, H., Christianson, D., Cheah, Y. W., Poindexter, C.,  
1069 Chen, J., Elbashandy, A., Humphrey, M., Isaac, P., Polidori, D., Ribeca, A., van Ingen, C., Zhang,  
1070 L., Amiro, B., Ammann, C., Arain, M. A., Ardö, J., Arkebauer, T., Arndt, S. K., Arriga, N.,  
1071 Aubinet, M., Aurela, M., Baldocchi, D., Barr, A., Beamesderfer, E., Marchesini, L. B., Bergeron,  
1072 O., Beringer, J., Bernhofer, C., Berveiller, D., Billesbach, D., Black, T. A., Blanken, P. D., Bohrer,  
1073 G., Boike, J., Bolstad, P. V., Bonal, D., Bonnefond, J. M., Bowling, D. R., Bracho, R., Brodeur, J.,  
1074 Brümmer, C., Buchmann, N., Burban, B., Burns, S. P., Buysse, P., Cale, P., Cavagna, M., Cellier,  
1075 P., Chen, S., Chini, I., Christensen, T. R., Cleverly, J., Collalti, A., Consalvo, C., Cook, B. D.,  
1076 Cook, D., Coursolle, C., Cremonese, E., Curtis, P. S., D'Andrea, E., da Rocha, H., Dai, X., Davis,  
1077 K. J., De Cinti, B., de Grandcourt, A., De Ligne, A., De Oliveira, R. C., Delpierre, N., Desai, A.  
1078 R., Di Bella, C. M., di Tommasi, P., Dolman, H., Domingo, F., Dong, G., Dore, S., Duce, P.,  
1079 Dufrêne, E., Dunn, A., Dušek, J., Eamus, D., Eichelmann, U., ElKhidir, H. A. M., Eugster, W.,  
1080 Ewenz, C. M., Ewers, B., Famulari, D., Fares, S., Feigenwinter, I., Feitz, A., Fensholt, R., Filippa,  
1081 G., Fischer, M., Frank, J., Galvagno, M., Gharun, M., Gianelle, D., et al.: The FLUXNET2015  
1082 dataset and the ONEFlux processing pipeline for eddy covariance data, *Scientific data*, 7, 225,  
1083 <https://doi.org/10.1038/s41597-020-0534-3>, 2020.
- 1084 Peñuelas, J., Ciais, P., Canadell, J. G., Janssens, I. A., Fernández-Martínez, M., Carnicer, J.,  
1085 Obersteiner, M., Piao, S., Vautard, R., and Sardans, J.: Shifting from a fertilization-dominated to a  
1086 warming-dominated period, *Nature Ecology and Evolution*, 1, 1438–1445,  
1087 <https://doi.org/10.1038/s41559-017-0274-8>, 2017.
- 1088 Piao, S., Wang, X., Park, T., Chen, C., Lian, X., He, Y., Bjerke, J. W., Chen, A., Ciais, P.,  
1089 Tømmervik, H., Nemani, R. R., and Myneni, R. B.: Characteristics, drivers and feedbacks of  
1090 global greening, *Nature Reviews Earth and Environment*, 1, 14–27,  
1091 <https://doi.org/10.1038/s43017-019-0001-x>, 2020.
- 1092 Prentice, I. C., Dong, N., Gleason, S. M., Maire, V., and Wright, I. J.: Balancing the costs of carbon  
1093 gain and water transport: testing a new theoretical framework for plant functional ecology,  
1094 *Ecology Letters*, 17, 82–91, <https://doi.org/10.1111/ele.12211>, 2014.



- 1095 Reich, P. B., Hobbie, S. E., and Lee, T. D.: Plant growth enhancement by elevated CO<sub>2</sub> eliminated  
1096 by joint water and nitrogen limitation, *Nature Geoscience*, 7, 920–924,  
1097 <https://doi.org/10.1038/ngeo2284>, 2014.
- 1098 Reichstein, M., Camps-Valls, G., Stevens, B., Jung, M., Denzler, J., Carvalhais, N., and Prabhat:  
1099 Deep learning and process understanding for data-driven Earth system science, *Nature*, 566,  
1100 195–204, <https://doi.org/10.1038/s41586-019-0912-1>, 2019.
- 1101 Ruehr, S., Keenan, T. F., Williams, C., Zhou, Y., Lu, X., Bastos, A., Canadell, J. G., Prentice, I. C.,  
1102 Sitch, S., and Terrer, C.: Evidence and attribution of the enhanced land carbon sink, *Nat Rev*  
1103 *Earth Environ*, 1–17, <https://doi.org/10.1038/s43017-023-00456-3>, 2023.
- 1104 Running, S., Mu, Q., and Zhao, M.: MOD17A2H MODIS/Terra Gross Primary Productivity 8-Day  
1105 L4 Global 500m SIN Grid V006, <https://doi.org/10.5067/MODIS/MOD17A2H.006>, 2015.
- 1106 Ryu, Y., Jiang, C., Kobayashi, H., and Detto, M.: MODIS-derived global land products of shortwave  
1107 radiation and diffuse and total photosynthetically active radiation at 5 km resolution from 2000,  
1108 *Remote Sensing of Environment*, 204, 812–825, <https://doi.org/10.1016/j.rse.2017.09.021>,  
1109 2018.
- 1110 Ryu, Y., Berry, J. A., and Baldocchi, D. D.: What is global photosynthesis? History, uncertainties and  
1111 opportunities, *Remote Sensing of Environment*, 223, 95–114,  
1112 <https://doi.org/10.1016/j.rse.2019.01.016>, 2019.
- 1113 Sabater, J. M.: ERA5-Land monthly averaged data from 1981 to present., Copernicus Climate  
1114 Change Service (C3S) Climate Data Store (CDS), <https://doi.org/doi:10.24381/cds.68d2bb30>,  
1115 2019.
- 1116 Schaaf, C. and Wang, Z.: MCD43C4 MODIS/Terra+Aqua BRDF/Albedo Nadir BRDF-Adjusted  
1117 Ref Daily L3 Global 0.05Deg CMG V006 [Data set], NASA EOSDIS Land Processes DAAC.,  
1118 <https://doi.org/10.5067/MODIS/MCD43C4.006>, 2015.
- 1119 Schwalm, C. R., Anderegg, W. R. L., Michalak, A. M., Fisher, J. B., Biondi, F., Koch, G., Litvak, M.,  
1120 Ogle, K., Shaw, J. D., Wolf, A., Huntzinger, D. N., Schaefer, K., Cook, R., Wei, Y., Fang, Y.,  
1121 Hayes, D., Huang, M., Jain, A., and Tian, H.: Global patterns of drought recovery, *Nature*, 548,  
1122 202–205, <https://doi.org/10.1038/nature23021>, 2017.
- 1123 Smith, W. K., Reed, S. C., Cleveland, C. C., Ballantyne, A. P., Anderegg, W. R. L., Wieder, W. R.,  
1124 Liu, Y. Y., and Running, S. W.: Large divergence of satellite and Earth system model estimates of  
1125 global terrestrial CO<sub>2</sub> fertilization, *Nature Climate Change*, 6, 306–310,  
1126 <https://doi.org/10.1038/nclimate2879>, 2016.
- 1127 Still, C. J., Berry, J. A., Collatz, G. J., and DeFries, R. S.: Global distribution of C<sub>3</sub> and C<sub>4</sub>  
1128 vegetation: Carbon cycle implications, *Global Biogeochemical Cycles*, 17,  
1129 <https://doi.org/10.1029/2001gb001807>, 2003.
- 1130 Still, C. J., Berry, J. A., Collatz, G. J., and DeFries, R. S.: ISLSCP II C<sub>4</sub> Vegetation Percentage, in:  
1131 Hall, Forrest G., G. Collatz, B. Meeson, S. Los, E. Brown de Colstoun, and D. Landis (eds.).  
1132 ISLSCP Initiative II Collection. Data set., <http://dx.doi.org/10.3334/ORNLDAAC/932>, 2009.



- 1133 Stocker, B. D., Zscheischler, J., Keenan, T. F., Prentice, I. C., Peñuelas, J., and Seneviratne, S. I.:  
1134 Quantifying soil moisture impacts on light use efficiency across biomes, *New Phytologist*, 218,  
1135 1430–1449, <https://doi.org/10.1111/nph.15123>, 2018.
- 1136 Stocker, B. D., Zscheischler, J., Keenan, T. F., Prentice, I. C., Seneviratne, S. I., and Peñuelas, J.:  
1137 Drought impacts on terrestrial primary production underestimated by satellite monitoring,  
1138 *Nature Geoscience*, 12, 264–270, <https://doi.org/10.1038/s41561-019-0318-6>, 2019.
- 1139 Stocker, B. D., Tumber-Dávila, S. J., Konings, A. G., Anderson, M. C., Hain, C., and Jackson, R. B.:  
1140 Global patterns of water storage in the rooting zones of vegetation, *Nat. Geosci.*, 16, 250–256,  
1141 <https://doi.org/10.1038/s41561-023-01125-2>, 2023.
- 1142 Terrer, C., Jackson, R. B., Prentice, I. C., Keenan, T. F., Kaiser, C., Vicca, S., Fisher, J. B., Reich, P.  
1143 B., Stocker, B. D., Hungate, B. A., Peñuelas, J., McCallum, I., Soudzilovskaia, N. A., Cernusak, L.  
1144 A., Talhelm, A. F., Van Sundert, K., Piao, S., Newton, P. C. D., Hovenden, M. J., Blumenthal, D.  
1145 M., Liu, Y. Y., Müller, C., Winter, K., Field, C. B., Viechtbauer, W., Van Lissa, C. J., Hoosbeek,  
1146 M. R., Watanabe, M., Koike, T., Leshyk, V. O., Polley, H. W., and Franklin, O.: Nitrogen and  
1147 phosphorus constrain the CO<sub>2</sub> fertilization of global plant biomass, *Nature Climate Change*, 9,  
1148 684–689, <https://doi.org/10.1038/s41558-019-0545-2>, 2019.
- 1149 Thoning, K. W., Crotwell, A. M., and Mund, J. W.: Atmospheric Carbon Dioxide Dry Air Mole  
1150 Fractions from continuous measurements at Mauna Loa, Hawaii, Barrow, Alaska, American  
1151 Samoa and South Pole. 1973-2020, Version 2021-08-09, National Oceanic and Atmospheric  
1152 Administration (NOAA), Global Monitoring Laboratory (GML), Boulder, Colorado, USA,  
1153 <https://doi.org/10.15138/yaf1-bk21>, 2021.
- 1154 Tramontana, G., Ichii, K., Camps-Valls, G., Tomelleri, E., and Papale, D.: Uncertainty analysis of  
1155 gross primary production upscaling using Random Forests, remote sensing and eddy covariance  
1156 data, *Remote Sensing of Environment*, 168, 360–373, <https://doi.org/10.1016/j.rse.2015.07.015>,  
1157 2015.
- 1158 Tramontana, G., Jung, M., Schwalm, C. R., Ichii, K., Camps-Valls, G., Ráduly, B., Reichstein, M.,  
1159 Arain, M. A., Cescatti, A., Kiely, G., Merbold, L., Serrano-Ortiz, P., Sickert, S., Wolf, S., and  
1160 Papale, D.: Predicting carbon dioxide and energy fluxes across global FLUXNET sites with  
1161 regression algorithms, *Biogeosciences*, 13, 4291–4313, [https://doi.org/10.5194/bg-13-4291-](https://doi.org/10.5194/bg-13-4291-2016)  
1162 2016, 2016.
- 1163 Ueyama, M., Ichii, K., Kobayashi, H., Kumagai, T., Beringer, J., Merbold, L., Euskirchen, E. S.,  
1164 Hirano, T., Marchesini, L. B., Baldocchi, D., Saitoh, T. M., Mizoguchi, Y., Ono, K., Kim, J.,  
1165 Varlagin, A., Kang, M., Shimizu, T., Kosugi, Y., Bret-Harte, M. S., Machimura, T., Matsuura, Y.,  
1166 Ohta, T., Takagi, K., Takanashi, S., and Yasuda, Y.: Inferring CO<sub>2</sub> fertilization effect based on  
1167 global monitoring land-atmosphere exchange with a theoretical model, *Environmental Research*  
1168 *Letters*, 15, 84009, <https://doi.org/10.1088/1748-9326/ab79e5>, 2020.
- 1169 Villarreal, S. and Vargas, R.: Representativeness of FLUXNET Sites Across Latin America, *Journal*  
1170 *of Geophysical Research: Biogeosciences*, 126, e2020JG006090,  
1171 <https://doi.org/10.1029/2020JG006090>, 2021.





- 1172 Walker, A. P., De Kauwe, M. G., Bastos, A., Belmecheri, S., Georgiou, K., Keeling, R. F.,  
1173 McMahon, S. M., Medlyn, B. E., Moore, D. J. P., Norby, R. J., Zaehle, S., Anderson-Teixeira, K.  
1174 J., Battipaglia, G., Brienen, R. J. W., Cabugao, K. G., Cailleret, M., Campbell, E., Canadell, J. G.,  
1175 Ciais, P., Craig, M. E., Ellsworth, D. S., Farquhar, G. D., Fatichi, S., Fisher, J. B., Frank, D. C.,  
1176 Graven, H., Gu, L., Haverd, V., Heilman, K., Heimann, M., Hungate, B. A., Iversen, C. M., Joos,  
1177 F., Jiang, M., Keenan, T. F., Knauer, J., Körner, C., Leshyk, V. O., Leuzinger, S., Liu, Y.,  
1178 MacBean, N., Malhi, Y., McVicar, T. R., Penuelas, J., Pongratz, J., Powell, A. S., Riutta, T., Sabot,  
1179 M. E. B., Schleucher, J., Sitch, S., Smith, W. K., Sulman, B., Taylor, B., Terrer, C., Torn, M. S.,  
1180 Treseder, K. K., Trugman, A. T., Trumbore, S. E., van Mantgem, P. J., Voelker, S. L., Whelan, M.  
1181 E., and Zuidema, P. A.: Integrating the evidence for a terrestrial carbon sink caused by increasing  
1182 atmospheric CO<sub>2</sub>, *New Phytologist*, 229, 2413–2445, <https://doi.org/10.1111/nph.16866>, 2021.
- 1183 Walther, S., Besnard, S., Nelson, J. A., El-Madany, T. S., Migliavacca, M., Weber, U., Carvalhais, N.,  
1184 Ermida, S. L., Brümmer, C., Schrader, F., Prokushkin, A. S., Panov, A. V., and Jung, M.:  
1185 Technical note: A view from space on global flux towers by MODIS and Landsat: the  
1186 FluxnetEO data set, *Biogeosciences*, 19, 2805–2840, <https://doi.org/10.5194/bg-19-2805-2022>,  
1187 2022.
- 1188 Wan, Z., Hook, S., and Hulley, G.: MOD11A1 MODIS/Terra Land Surface  
1189 Temperature/Emissivity Daily L3 Global 1km SIN Grid V006 [Data set], NASA EOSDIS Land  
1190 Processes DAAC, <https://doi.org/10.5067/MODIS/MOD11A1.006>, 2015a.
- 1191 Wan, Z., Hook, S., and Hulley, G.: MYD11A1 MODIS/Aqua Land Surface  
1192 Temperature/Emissivity Daily L3 Global 1km SIN Grid V006 [Data set], NASA EOSDIS Land  
1193 Processes DAAC, <https://doi.org/10.5067/MODIS/MYD11A1.006>, 2015b.
- 1194 Wang, H., Prentice, I. C., Keenan, T. F., Davis, T. W., Wright, I. J., Cornwell, W. K., Evans, B. J.,  
1195 and Peng, C.: Towards a universal model for carbon dioxide uptake by plants, *Nature Plants*, 3,  
1196 734–741, <https://doi.org/10.1038/s41477-017-0006-8>, 2017.
- 1197 Warm Winter 2020 Team and ICOS Ecosystem Thematic Centre.: Warm Winter 2020 ecosystem  
1198 eddy covariance flux product for 73 stations in FLUXNET-Archive format—release 2022-1  
1199 (Version 1.0), <https://doi.org/10.18160/2G60-ZHAK>, 2022.
- 1200 Wenzel, S., Cox, P. M., Eyring, V., and Friedlingstein, P.: Projected land photosynthesis constrained  
1201 by changes in the seasonal cycle of atmospheric CO<sub>2</sub>, *Nature*, 538, 499–501,  
1202 <https://doi.org/10.1038/nature19772>, 2016.
- 1203 Xiao, J., Zhuang, Q., Baldocchi, D. D., Law, B. E., Richardson, A. D., Chen, J., Oren, R., Starr, G.,  
1204 Noormets, A., Ma, S., Verma, S. B., Wharton, S., Wofsy, S. C., Bolstad, P. V., Burns, S. P., Cook,  
1205 D. R., Curtis, P. S., Drake, B. G., Falk, M., Fischer, M. L., Foster, D. R., Gu, L., Hadley, J. L.,  
1206 Hollinger, D. Y., Katul, G. G., Litvak, M., Martin, T. A., Matamala, R., McNulty, S., Meyers, T.  
1207 P., Monson, R. K., Munger, J. W., Oechel, W. C., Paw U, K. T., Schmid, H. P., Scott, R. L., Sun,  
1208 G., Suyker, A. E., and Torn, M. S.: Estimation of net ecosystem carbon exchange for the  
1209 conterminous United States by combining MODIS and AmeriFlux data, *Agricultural and Forest  
1210 Meteorology*, 148, 1827–1847, <https://doi.org/10.1016/j.agrformet.2008.06.015>, 2008.



- 1211 Xie, X., Chen, J. M., Yuan, W., Guan, X., Jin, H., and Leng, J.: A Practical Algorithm for Correcting  
1212 Topographical Effects on Global GPP Products, *Journal of Geophysical Research:*  
1213 *Biogeosciences*, 128, e2023JG007553, <https://doi.org/10.1029/2023JG007553>, 2023.
- 1214 Xie, Y., Gibbs, H. K., and Lark, T. J.: Landsat-based Irrigation Dataset (LANID): 30m resolution  
1215 maps of irrigation distribution, frequency, and change for the US, 1997–2017, *Earth System*  
1216 *Science Data*, 13, 5689–5710, <https://doi.org/10.5194/essd-13-5689-2021>, 2021.
- 1217 Yan, K., Park, T., Yan, G., Chen, C., Yang, B., Liu, Z., Nemani, R. R., Knyazikhin, Y., and Myneni,  
1218 R. B.: Evaluation of MODIS LAI/FPAR product collection 6. Part 1: Consistency and  
1219 improvements, *Remote Sensing*, 8, 1–16, <https://doi.org/10.3390/rs8050359>, 2016a.
- 1220 Yan, K., Park, T., Yan, G., Liu, Z., Yang, B., Chen, C., Nemani, R. R., Knyazikhin, Y., and Myneni,  
1221 R. B.: Evaluation of MODIS LAI/FPAR product collection 6. Part 2: Validation and  
1222 intercomparison, *Remote Sensing*, 8, 460, <https://doi.org/10.3390/rs8060460>, 2016b.
- 1223 Yang, F., Ichii, K., White, M. A., Hashimoto, H., Michaelis, A. R., Votava, P., Zhu, A. X., Huete, A.,  
1224 Running, S. W., and Nemani, R. R.: Developing a continental-scale measure of gross primary  
1225 production by combining MODIS and AmeriFlux data through Support Vector Machine  
1226 approach, *Remote Sensing of Environment*, 110, 109–122,  
1227 <https://doi.org/10.1016/j.rse.2007.02.016>, 2007.
- 1228 Yang, R., Wang, J., Zeng, N., Sitch, S., Tang, W., McGrath, M. J., Cai, Q., Liu, D., Lombardozzi, D.,  
1229 Tian, H., Jain, A. K., and Han, P.: Divergent historical GPP trends among state-of-the-art multi-  
1230 model simulations and satellite-based products, *Earth System Dynamics*, 13, 833–849,  
1231 <https://doi.org/10.5194/esd-13-833-2022>, 2022.
- 1232 Yuan, H., Dai, Y., Xiao, Z., Ji, D., and Shangguan, W.: Reprocessing the MODIS Leaf Area Index  
1233 products for land surface and climate modelling, *Remote Sensing of Environment*, 115, 1171–  
1234 1187, <https://doi.org/10.1016/j.rse.2011.01.001>, 2011.
- 1235 Zeng, J., Matsunaga, T., Tan, Z.-H., Saigusa, N., Shirai, T., Tang, Y., Peng, S., and Fukuda, Y.:  
1236 Global terrestrial carbon fluxes of 1999–2019 estimated by upscaling eddy covariance data with a  
1237 random forest, *Sci Data*, 7, 313, <https://doi.org/10.1038/s41597-020-00653-5>, 2020.
- 1238 Zeng, N., Zhao, F., Collatz, G. J., Kalnay, E., Salawitch, R. J., West, T. O., and Guanter, L.:  
1239 Agricultural Green Revolution as a driver of increasing atmospheric CO<sub>2</sub> seasonal amplitude,  
1240 *Nature*, 515, 394–397, <https://doi.org/10.1038/nature13893>, 2014.
- 1241 Zhang, Y.: A global spatially contiguous solar-induced fluorescence (CSIF) dataset using neural  
1242 networks (2000–2020), National Tibetan Plateau Data Center,  
1243 <https://doi.org/10.11888/Ecolo.tpdc.271751>, 2021.
- 1244 Zhang, Y., Joiner, J., Hamed Alemohammad, S., Zhou, S., and Gentine, P.: A global spatially  
1245 contiguous solar-induced fluorescence (CSIF) dataset using neural networks, *Biogeosciences*, 15,  
1246 5779–5800, <https://doi.org/10.5194/bg-15-5779-2018>, 2018.
- 1247 Zheng, Y., Shen, R., Wang, Y., Li, X., Liu, S., Liang, S., Chen, J. M., Ju, W., Zhang, L., and Yuan,  
1248 W.: Improved estimate of global gross primary production for reproducing its long-Term



- 1249 variation, 1982-2017, Earth System Science Data, 12, 2725–2746, <https://doi.org/10.5194/essd->  
1250 12-2725-2020, 2020.
- 1251 Zhu, Z., Piao, S., Myneni, R. B., Huang, M., Zeng, Z., Canadell, J. G., Ciais, P., Sitch, S.,  
1252 Friedlingstein, P., Arneeth, A., Cao, C., Cheng, L., Kato, E., Koven, C., Li, Y., Lian, X., Liu, Y.,  
1253 Liu, R., Mao, J., Pan, Y., Peng, S., Peuelas, J., Poulter, B., Pugh, T. A. M., Stocker, B. D., Viovy,  
1254 N., Wang, X., Wang, Y., Xiao, Z., Yang, H., Zaehle, S., and Zeng, N.: Greening of the Earth and  
1255 its drivers, Nature Climate Change, 6, 791–795, <https://doi.org/10.1038/nclimate3004>, 2016.
- 1256